



A novel (Ti/Ce)UiO-X MOFs@TiO₂ heterojunction for enhanced photocatalytic performance: Boosting via Ce⁴⁺/Ce³⁺ and Ti⁴⁺/Ti³⁺ redox mediators

Patrycja Parnicka^{a,*}, Wojciech Lisowski^b, Tomasz Klimczuk^{c,d}, Alicja Mikołajczyk^{e,f},
Adriana Zaleska-Medynska^{a,*}

^a Department of Environmental Technology, Faculty of Chemistry, University of Gdansk, 80-308 Gdansk, Poland

^b Institute of Physical Chemistry, Polish Academy of Sciences, 01-224 Warsaw, Poland

^c Faculty of Applied Physics and Mathematics, Gdansk University of Technology, 80-233 Gdansk, Poland

^d Advanced Materials Centre, Gdansk University of Technology, 80-233 Gdansk, Poland

^e Laboratory of Environmental Chemometrics, Faculty of Chemistry, University of Gdansk, 80-308 Gdansk, Poland

^f QSAR Lab Ltd., Trzy Lipy 3, 80-172 Gdansk, Poland

ARTICLE INFO

Keywords:

Metal-organic framework
Bimetallic Ti/Ce
Ligand substitution
Titanium dioxide
Density Functional Theory Simulations

ABSTRACT

Titanium-substituted cerium-oxo-based UiO MOFs with terephthalate linkers modified by various groups (–Br, –NH₂, –NO₂) or their derivatives (N-heterocyclic or biphenyl groups) were combined with titanium dioxide in a multistep route to obtain a core-shell-like architecture. DFT simulations showed that Ce- and bimetallic Ti/Ce-MOFs exhibited different charge compensation. Extended characterization revealed the formation of heterojunctions between the (Ti/Ce)UiO-X MOFs and TiO₂ nanoflowers, suitable band edge positions, and high specific surface area and porosity, which resulted in effective electron transfer and excellent photocatalytic activity. The photoactivity of the (Ti/Ce)UiO-X@TiO₂ composites for hydrogen production or phenol degradation varied according to the order –NH₂ > biphenyl > –N– > –H > –Br > –NO₂ > pristine TiO₂ or –Br > –NH₂ > –NO₂ > –N– > –H > biphenyl > pristine TiO₂. The photocatalytic hydrogen production rate of (Ti/Ce)UiO-66-NH₂@TiO₂ was 4724 and 19.3 μmol·g^{–1}·h^{–1} after 4 h of UV-Vis and visible light irradiation, which were 79 and 19 times higher than that of pristine rutile, respectively.

1. Introduction

Some of the most important goals of the European Union's long-term strategy are to reach the standards set by the Paris Agreement on the elimination of air, water, and soil pollutants and to implement a hydrogen strategy for a climate-natural Europe by 2050 [1]. Thus, new materials that may remove pollutants from different environmental media while producing hydrogen are being intensively explored [2,3]. Metal-organic frameworks (MOFs) have been recognized as compelling platforms for the development of photocatalytic applications because of their structural diversity and functional tunability. Cavka et al. [4] at the University of Oslo first reported the UiO-66 MOF constructed from terephthalate ligands and Zr(IV)-oxo clusters; however, this material has a wide (~3.1–4.6 eV) HOMO-LUMO gap (gap between the highest occupied molecular orbital and lowest unoccupied molecular orbital

energy levels), and is relatively inefficient under visible light [4]. Additionally, it was reported that (Zr)UiO-66 was unable to promote visible-light-driven H₂ generation even with the aid of a cocatalyst [5]. Recently, enclosing cerium-oxo clusters within an MOF has been demonstrated as a promising approach to achieve a photocatalyst with more efficient solar energy conversion, wherein the MOF exhibits semiconductor behaviours with electron transfer from photoexcited organic linkers to metal-oxo clusters (LCCTs). Moreover, the large surface areas and small photocatalytic centres (small cerium-oxo clusters) of MOFs are advantageous for efficient photocatalysts [6]. More importantly, the HOMO-LUMO gap of the MOFs can be adjusted by varying and decorating the organic linkers, thereby increasing the range of absorbed visible light irradiation [6,7]. Additionally, the functional groups in MOFs are helpful for promoting the adsorption and diffusion of reactants and products. However, unbalanced electron (e[–]) and hole

* Corresponding authors.

E-mail addresses: patrycja.parnicka@phdstud.ug.edu.pl (P. Parnicka), adriana.zaleska-medynska@ug.edu.pl (A. Zaleska-Medynska).

<https://doi.org/10.1016/j.apcatb.2022.121349>

Received 22 December 2021; Received in revised form 7 March 2022; Accepted 23 March 2022

Available online 25 March 2022

0926-3373/© 2022 Elsevier B.V. All rights reserved.

(h^+) mobilities and rapid recombination of charge carriers are still major issues for single-component photocatalysts, including MOFs. Strategies to solve this problem include preparing MOFs doped with a metal to modify the band structure of the photocatalyst or coupling them with another semiconductor material to form a heterojunction that promotes the transfer of photoinduced charge carriers located at the interface and creates abundant active sites for the surface reaction. For example, Zhang et al. [8] and Wang et al. [9] confirmed that the incorporation of Ti into (Ce)UiO-66 and (Zr)UiO-66-NH₂ improved the photocatalytic reduction properties through a Ti-mediated electron transfer mechanism, where the electron charge transfer of an excited organic ligand or ligand to metal-oxo clusters is promoted by the Ti-mediator species present in the MOF structure [8,9]. The creation of heterojunctions using MOFs (e.g., NH₂-MIL-53(Al)/CdS [10], Au@thiol-UiO66(Zr)/ZnIn₂S₄ [11], H₃PW₁₂O₄₀/(Zr)PCN-222 [12], and ZIF-8/TiO₂ [13]) has been studied often, and these heterojunctions show excellent photocatalytic activity for the degradation of pollutants, hydrogen production, and carbon dioxide reduction. A composite consisting of two and more components exhibits physical or chemical properties that are significantly different from those of the individual components. The coupling of MOFs and semiconductor photocatalysts to fabricate hybrid composites offers many excellent opportunities in photocatalytic processes because (1) MOFs can act as photosensitizers to achieve efficient light utilization; (2) photoexcited electrons can be easily transferred from organic ligands to metal ions or clusters; and (3) semiconductor photocatalysts (such as TiO₂) act as the primary photocatalysts, and MOFs act as cocatalysts [14]. Additionally, the combination of MOFs and semiconductor photocatalysts can overcome the drawbacks of each material alone while maintaining their advantages. Zhang et al. [13] prepared hollow ZIF-8/@TiO₂ nanospheres, which achieved a higher hydrogen evolution rate than pristine samples due to the efficient charge carrier separation between ZIF-8 and TiO₂ via electron injection [13]. However, core-shell MIL-125-NH₂@TiO₂ structures exhibited some advantages in photocatalytic hydrogen production due to the mesoporous framework that provides more active sites and enhanced photocatalytic activity (70 times higher than that of pristine MOF) with the aid of quick mass and charge transfer [15].

In summary, no studies have systematically considered metal substitution, linker modification in (Ce)UiO-X MOFs, heterojunction formation with other materials, or the use of the above hybrid material for photocatalytic applications. Thus, for the first time, titanium-doped cerium-oxo-based UiO MOFs with terephthalate linkers modified by various X groups (X = -Br, -NH₂, -NO₂) or their derivatives (N-heterocyclic or biphenyl groups) combined with titanium dioxide were designed and synthesized via a multistep route. The density functional theory (DFT) calculations were performed to compare the energies of MOFs containing a single Ce or a bimetallic Ti/Ce centre for different charge compensation choices. The prepared hybrid materials were applied to the photoreduction of chromium(VI), photodegradation of phenol, and hydrogen generation. To propose a possible photocatalytic mechanism of the (Ti/Ce)UiO-X/TiO₂ composite photocatalysts, photodegradation experiments in the presence of scavengers, hydroxyl radical tests with terephthalic acid, and superoxide radical tests with nitroblue tetrazolium chloride as well as the action spectra (wavelength-dependent apparent quantum efficiency) were performed.

2. Experimental details

2.1. Materials

All chemicals were purchased from Sigma-Aldrich (Germany), POCH S. A (Poland), or STANLAB (Poland) and used without further purification.

2.2. Preparation of TiO₂

TiO₂ was synthesized by the hydrothermal method according to a previously reported procedure [16]. A mixture of tetrabutyl titanate (0.1 mol, 34 g, 98%) and hydrochloric acid (35 g, 38%) was mixed in a beaker. After 10 min, the mixture was transferred to an autoclave and stored at 170 °C for 24 h. After the autoclave was cooled to room temperature, the precipitate was separated from the suspension by centrifugation and washed with ethanol and water, followed by drying at 60 °C overnight.

2.3. Synthesis of (Ce)UiO-X@TiO₂

The linker precursor (terephthalic acid (H₂BDC or TPA), 2-bromoterephthalic acid (Br-H₂BDC), 2-nitroteterephthalic acid (NO₂-H₂BDC), 2-aminoteterephthalic acid (NH₂-H₂BDC), pyridine-2,5-dicarboxylic acid (H₂PDC), and biphenyl-4,4'-dicarboxylic acid (H₂BPDC), see Table S1, 0.65 mmol) was dissolved in *N,N*-dimethylformamide (DMF, 3.75 mL), and the required amount of TiO₂ was added to the mixture. After 30 min of stirring at room temperature, an aqueous 0.2665 M solution of (NH₄)₂Ce(NO₃)₆ was added and then transferred to Pyrex glass reaction tubes. The glass reactor was sealed and heated using an aluminium heater block while stirring for 30 min at 100 °C. After the reaction, (Ce)UiO-X@TiO₂ was purified by washing with DMF and ethanol. The resulting solids were dried under vacuum at 80 °C. To fabricate amino-tagged UiO-66 MOF, cerium clusters [Ce₆O₄(OH)₄(NH₃-CH₂COO)₈(-NO₃)₄(H₂O)₆Cl₈·8H₂O] were first prepared according to the literature [17] and were used in the above procedure in place of the cerium precursor (NH₄)₂Ce(NO₃)₆. The initial step of the preliminary experiment was to select an appropriate (Ce)UiO-X MOF content for the synthesis of the MOF@TiO₂ composites (see Table S2 in the supplementary material for more detailed data). The mass percentages of (Ce)UiO-X MOFs in the composite were set to 10 wt% based on the ratio between the masses of the MOF precursors and TiO₂ used in the synthesis.

2.4. Synthesis of (Ti/Ce)UiO-X@TiO₂

TiCp₂Cl₂ (19.5 mg, 0.4 mmol equiv to Ti) and (Ce)UiO-X@TiO₂ (260 mg, 0.4 mmol equiv to Ce) were mixed in 50 mL of DMF with vigorous stirring. The obtained uniform slurry was transferred to a 50 mL round-bottom flask, kept at 100 °C for 3 h, and then cooled to ambient temperature. The product was collected by centrifugation and washed with DMF and ethanol three times. The resultant (Ti/Ce)UiO-X@TiO₂ was collected from ethanol by centrifugation and then dried under vacuum at 80 °C before use.

2.5. Characterization techniques

The morphologies of the prepared samples were investigated by field emission scanning electron microscopy (JEOL FE-SEM JSM-7610 F). Powder X-ray diffraction (PXRD) was used to confirm the crystal structure and calculate the lattice parameters of TiO₂ and the MOFs. The PXRD patterns were collected using a D2 Phaser (Bruker) diffractometer equipped with a CuK α radiation source (λ = 1.5406 Å) and an XE-T detector. The lattice parameters were estimated by the LeBail profile method using High Score Plus software. Fourier transform infrared (FTIR) spectroscopy was performed at 8 cm⁻¹ resolution in the range of 400–4000 cm⁻¹ on a Nicolet iS10 FTIR spectrometer. The samples were prepared by diluting 10% of the photocatalyst in KBr. X-ray photoelectron spectroscopy (XPS) measurements were performed using a PHI 5000 VersaProbe™ Scanning ESCA Microprobe (ULVAC-PHI; Chigasaki Japan) instrument. The XPS spectra were recorded using monochromatic Al-K α radiation ($h\nu$ = 1486.6 eV) from an X-ray source operating at a 100 μ m spot size, 25 W and 15 kV. High-resolution (HR) XPS spectra were collected with an analyser pass energy of 23.5 eV and an energy step size of 0.1 eV. Casa XPS software (v.2.3.19, Casa Software

Ltd, Wilmslow, United Kingdom) was used to evaluate the XPS data. The binding energy scale was referenced to the C 1 s peak, where $BE = 284.8$ eV. For quantification, the PHI Multipak sensitivity factors and determined transmission function of the spectrometer were used. Thermogravimetric analysis (TGA) of the samples was performed on a Perkin-Elmer TG8000; the sample were heated from $30\text{ }^{\circ}\text{C}$ to $800\text{ }^{\circ}\text{C}$ under a nitrogen atmosphere at a rate of $10\text{ }^{\circ}\text{C}/\text{min}$. IR experiments were carried out using Bruker IFS66. The specific surface area (BET) and pore size distribution were determined on a Gemini analyser (Micromeritics) and were calculated from the adsorption and desorption branches of the isotherms, respectively, by applying the BET equation for the N_2 relative pressure range of $0.00001 < P/P_0 < 0.3$ and the Barrett-Joyner-Halenda (BJH) method for the pressure range of $0.03 < P/P_0 < 0.99$. The diffuse reflectance spectra (DRS) were recorded on a Shimadzu UV-Vis spectrophotometer (UV 2600) equipped with an integrating sphere. BaSO_4 was used as the reference. The obtained absorption spectra were recorded in the range of 250–850 nm with a scanning speed of 200 nm/min at room temperature. The photoluminescence (PL) properties were measured in the 300–700 nm range using a Perkin Elmer Ltd. An LS50B spectrophotometer equipped with a xenon discharge lamp as an excitation source and an R928 photomultiplier as a detector. The spectra were recorded with an excitation wavelength of 315 nm directed towards the sample surface at an angle of 90° .

2.6. Density functional theory simulations

The theoretical investigation of MOF structures was carried out with periodic density functional theory (DFT) using the plane-wave-basis Vienna *ab initio* simulation package (VASP) under the Kohn-Sham density functional theory (DFT) framework. The optimal bulk crystal structures of (Ti)UiO-66, (Ce)UiO-66 and (Ce/Ti)UiO-66 MOFs were computed using recently-developed the strongly constrained and appropriately normed SCAN meta-generalised gradient approximation with long-range van der Waals interactions from the revised Vydrov-van Voorhis nonlocal correlation functional (SCAN + rVV10) [18–21]. The total energy was converged to $< 1\text{ meV atom}^{-1}$ using a kinetic cut-off energy of 800 eV and an appropriate Γ -centred Monkhorst-Pack k-point mesh with a separation of 0.035 \AA^{-1} . Finally, ionic optimizations were performed until all the forces were below 0.02 eV \AA^{-1} . The band structure of pristine (Ce)UiO-66 MOF was computed using the hybrid HSE06 [22] using the optimal atomic structure obtained by SCAN + rVV10.

2.7. Measurement of photocatalytic activity

Photocatalytic tests under UV-Vis and visible light irradiation were investigated using a 1000 W Xenon lamp (Oriel 66021) equipped with a water IR cut-off filter. For the visible-light test activity, the light beam was passed through a GG420 filter to cut-off wavelengths shorter than 420 nm. The irradiation intensity was measured with an optical power meter (HAMAMATSU, C9536-01) and was $4\text{ mW}\cdot\text{cm}^{-2}$ for visible light irradiation. Batch glass photoreactors with a cooling jacket and a quartz window were used to study the photocatalytic evolution reactions. The photoreactor configurations with different dimensions are shown in Table S3 in the supplementary materials; reactor R2 was used for hydrogen evolution, while reactor R1 was used for phenol and chromium removal. The experimental procedure for the photodegradation hexavalent chromium anion in the form of $\text{Cr}_2\text{O}_7^{2-}$ (pH 3) was as follows: the prepared photocatalyst ($1\text{ g}\cdot\text{L}^{-1}$) was dispersed in a 25 mL of a 0.07 mM Cr(VI) solution. The reaction mixture was added to the photoreactor and then stirred for an additional 40 min (550 rpm) in the dark. The temperature of the suspension during photoirradiation was maintained at $10 \pm 0.5\text{ }^{\circ}\text{C}$ using a thermostatically controlled water bath. The temperature was selected so the results could be compared to those obtained in the phenol photodegradation process, as phenol

stripping does not occur at $10\text{ }^{\circ}\text{C}$. Next, the suspension was irradiated with a cut-off spectrum of light. At particular time intervals, 0.5 mL of sample was collected, and the photocatalyst particles were removed immediately by centrifugation. The Cr(VI) concentration was determined spectrophotometrically at 540 nm using diphenylcarbazide, according to ISO PN-EN 18,412. Hydrogen evolution from water under UV-Vis and visible irradiation, using TEOA as the sacrificial reagent, was evaluated as follows: the prepared photocatalyst ($1\text{ g}\cdot\text{L}^{-1}$) was dispersed in 80 mL of an aqueous solution containing 10% triethanolamine (TEOA; see the Supplementary Material for more information). The suspension was placed in a quartz photoreactor, which was tightly closed, and then magnetically stirred and degassed with N_2 for 1 h (550 rpm) in the dark to reach adsorption-desorption equilibrium. The temperature in the reactor during the process was maintained at $20 \pm 0.5\text{ }^{\circ}\text{C}$ using a thermostatically controlled water bath. Before irradiation was initiated, a reference sample was taken. The concentration of H_2 evolved was determined at regular time intervals of 1 h using a gas chromatograph (TRACE 1300, Thermo Scientific) equipped with a HayeSep Q (80/100) column and a thermal conductivity detector (TCD), with N_2 as the carrier gas. The samples (200 μL) were injected via a gas-tight syringe. Phenol degradation under visible light irradiation was investigated using the same photocatalytic setup as chromium photoreduction, and the experimental procedure was as follows: the prepared photocatalyst ($1\text{ g}\cdot\text{L}^{-1}$) was dispersed in a 25 mL aqueous 0.21 mM phenol solution. The reaction mixture was added to the photoreactor and then stirred for an additional 40 min (550 rpm) with constant aeration ($5\text{ dm}^3\cdot\text{h}^{-1}$). Thereafter, visible light irradiation was performed. The temperature of the suspension during photoirradiation was maintained at $10 \pm 0.5\text{ }^{\circ}\text{C}$ using a thermostatically controlled water bath. The phenol solution ($\sim 0.5\text{ mL}$) was retrieved at specific time intervals, filtered using a $0.2\text{ }\mu\text{m}$ syringe filter, and analysed. A high-performance liquid chromatography system (HPLC, Shimadzu) equipped with a Kinetex C18 column, a precolumn, and an SPD-M20A diode array detector ($\lambda = 205, 225, \text{ and } 254\text{ nm}$) was used to determine the concentrations of phenol and the intermediates in the solution. The mobile phase was composed of acetonitrile and 0.005% trifluoroacetic acid, and isocratic elution (20:80 (v:v)) was used with a constant flow rate. Action spectral measurements were performed for selected (Ti/Ce)UiO-66- NH_2 @ TiO_2 photocatalyst. Experiments were performed in a reactor at initial phenol and photocatalyst concentrations of 0.21 mM and $1\text{ g}\cdot\text{L}^{-1}$, respectively. The reaction mixture was irradiated at monochromatic wavelengths for 90 min ($\lambda = 400, 420, 440, 460\text{ nm}$), 180 min ($\lambda = 480, 500, 550\text{ nm}$), 360 min ($\lambda = 600, 650\text{ nm}$) using a tunable monochromatic light source (1000 W Xe lamp LSH602 and LOT-Quantum Design monochromator MSW306). The light intensity was measured using an optical power meter (ILT2400, International Light Technologies). The samples ($\sim 0.1\text{ mL}$) for HPLC analysis were collected at 30 or 60 min intervals. The apparent quantum efficiency (AQE) as a function of wavelength was calculated based on the ratio of the rate of electron consumption (rate of benzoquinone generation) to the flux of incident photons, assuming that two photons were required according to the reaction stoichiometry.

2.8. Determination of reactive species

The determination of hydroxyl radicals ($\cdot\text{OH}$) generated over the prepared samples during photocatalysis was performed by a fluorescence technique with terephthalic acid (TPA, 50 mM) [23]. The test was performed by employing an LS50B spectrophotometer (Perkin Elmer Ltd.) equipped with a Xenon discharge lamp and an R928 photomultiplier. The obtained solution was measured at an excitation wavelength of 315 nm. The generation of superoxide radicals ($\text{O}_2^{\cdot-}$) during irradiation was evaluated spectrophotometrically with nitroblue tetrazolium chloride (NBT, 0.025 mM) [24]. NBT, with an absorption maximum at 259 nm, reacts with superoxide radicals, resulting in a decrease in the NBT concentration analysed by detecting the absorption. The decrease in the NBT concentration is proportional to the number of

superoxide radicals produced. Redox species scavenging experiments were performed using benzoquinone, silver nitrate, ammonium oxalate, and *tert*-butanol. The aqueous phenol solution containing the above-mentioned scavengers ($C_0 = 0.21$ mM, 1:1) and photocatalyst was subjected to the same experimental procedure used for phenol photodegradation described in Section 2.3.

3. Results and discussion

The (Ti/Ce)UiO-X@TiO₂ hybrid material was obtained via a multi-step strategy that can be summarized as follows. Initially, TiO₂ microspheres were prepared by the solvothermal method of the hydrolysis of titanium(IV) butoxide. The (Ce)UiO-X MOF (X = functional group) shell was prepared by an in situ crystallization strategy in the presence of TiO₂ particles; this strategy involved solvothermal synthesis that used ammonium cerium(IV) nitrate as the cerium node and terephthalic acid with several substituents (–Br, –NO₂ or –NH₂) or their derivatives (N-heterocyclic or biphenyl groups) as the ligands. Subsequently, titanium was introduced via the cation exchange process and was achieved by the reaction between (Ce)UiO-X MOFs and titanocene dichloride in DMF. In general, the use of the layer-by-layer growth method for the MOF deposition process on TiO₂ semiconductors allowed linker groups to bind metal ions at the surface and vice versa. The growth mechanism

involves a reaction between preformed secondary building units (SBUs) and anchored surface groups [25]. Schematic diagrams for the fabrication of (Ti/Ce)UiO-X MOF-modified TiO₂ core-shell composites and a description of the prepared photocatalysts are shown in Fig. 1a and Table 1.

3.1. Theoretical calculations

To gain insight into the electronic properties of the investigated (Ti)UiO-66, (Ce)UiO-66, and (Ti/Ce)UiO-66 MOF materials, the electronic structures and partial density of states were calculated using the hybrid HSE06 hybrid functional implemented in the VASP package [22] and the optimal atomic structure carried out using SCAN + rVV10. The calculated PDOS structure and the highest occupied crystalline orbital (HOCO) for (Ti)UiO-66, (Ce)UiO-66, and (Ti/Ce)UiO-66 MOF structures are shown in Fig. 2a–c, and 2d–f, respectively. Since the position of the bands relative to the vacuum level is of importance for charge transfer processes, thus the vacuum aligned energy and the position of the band gap is presented in Fig. 2g. The calculated results indicated that the band gap value of (Zn)UiO-66 MOF is equal to 4.3 eV. The presence of Ti in the (Ti)UiO-66 MOF structure decrease the band gap to ~3.6 eV (Fig. 2a). In contrast, the presence of Ce in the (Ce)UiO-66 MOF structure result in the presence of Ce states that populates the band gap

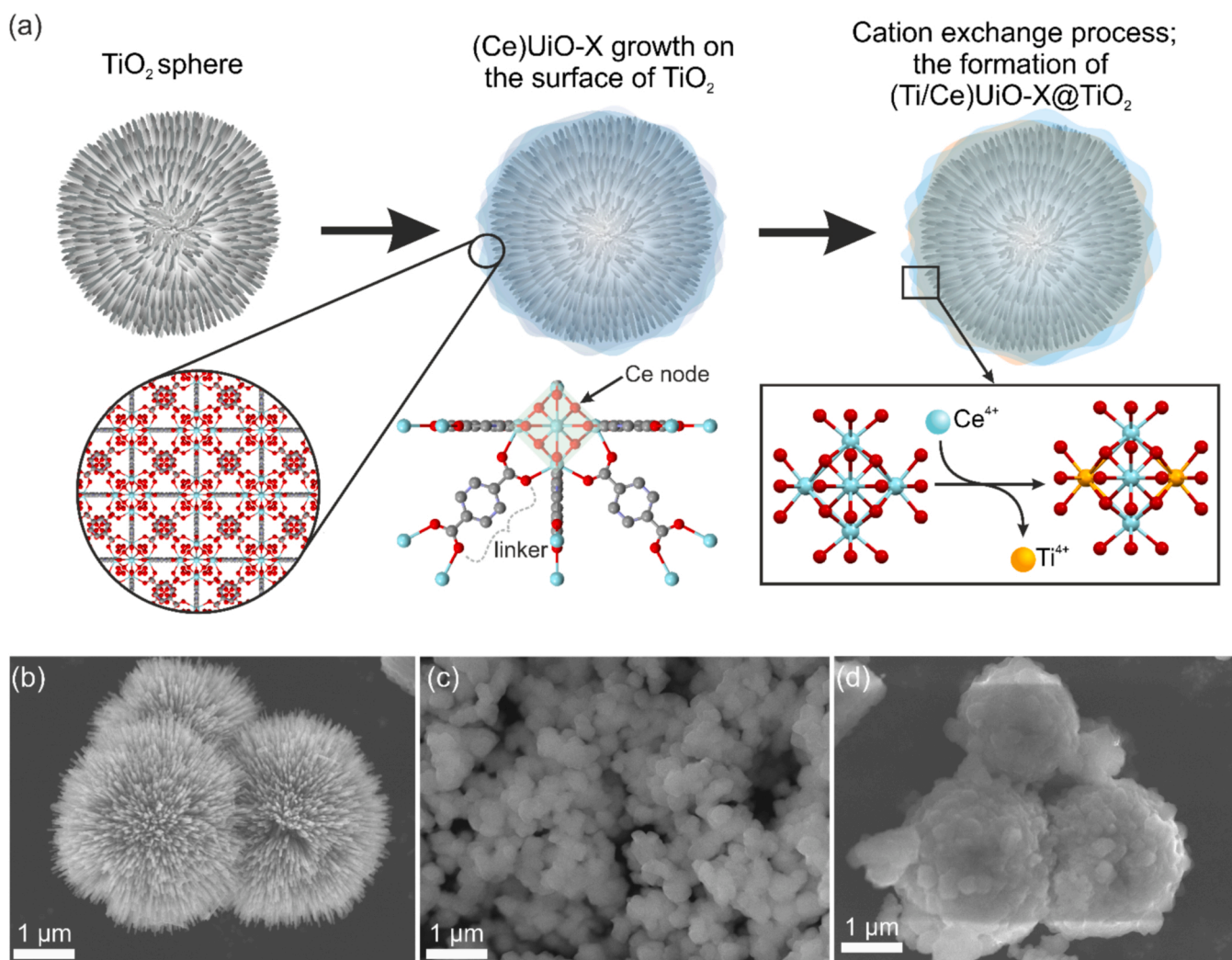


Fig. 1. (a) Schematic depicting the structure and formation process of (Ti/Ce)UiO-X MOF-modified TiO₂. Scanning electron microscopy images of (b) pristine TiO₂, (c) pristine (Ce)UiO MOFs, and (d) (Ce/Ti)UiO@TiO₂ composites. The (Ce)- and (Ti/Ce)UiO-66 MOF crystal structures were proposed using Mercury software based on literature reports [21].

Table 1
Description and physicochemical characterization of photocatalysts.

Sample	Metal ions type in MOFs	Linker type in MOFs	MOF content (wt.%)		XRD lattice parameters UiO MOFs a (Å)	Rutile TiO ₂		S _{BET} (m ² ·g ⁻¹)	Pore size (nm)	Pore volume (cm ³ ·g ⁻¹)
			Theoretical	Real contents of MOF (wt.%) based on TGA		a = b (Å)	c (Å)			
TiO ₂	None	None	0	0	–	4.5947 (1)	2.9570 (1)	14	1.83	0.01
(Ce)UiO-66	Ce	H ₂ BDC	100	100	21.4662(2)	–	–	793	1.94	0.38
(Ce)UiO-66-Br	Ce	Br-H ₂ BDC	100	100	21.3750(7)	–	–	599	1.91	0.29
(Ce)UiO-66-NO ₂	Ce	NO ₂ -H ₂ BDC	100	100	21.4536(3)	–	–	316	1.92	0.15
(Ce)UiO-66-NH ₂	Ce	NH ₂ -H ₂ BDC	100	100	21.4824(1)	–	–	186	1.88	0.09
(Ce)UiO-66-N	Ce	H ₂ PDC	100	100	21.4147(2)	–	–	147	1.92	0.07
(Ce)UiO-67	Ce	H ₂ BPDC	100	100	27.585(1)	–	–	585	1.91	0.03
(Ti/Ce)UiO-66	Ce, Ti	H ₂ BDC	100	100	21.4179(7)	–	–	454	1.94	0.22
(Ti/Ce)UiO-66-Br	Ce, Ti	Br-H ₂ BDC	100	100	21.4891(4)	–	–	263	1.92	0.13
(Ti/Ce)UiO-66-NO ₂	Ce, Ti	NO ₂ -H ₂ BDC	100	100	21.4955(3)	–	–	236	1.94	0.12
(Ti/Ce)UiO-66-NH ₂	Ce, Ti	NH ₂ -H ₂ BDC	100	100	21.48(2)	–	–	133	1.83	0.06
(Ti/Ce)UiO-66-N	Ce, Ti	H ₂ PDC	100	100	21.4416(2)	–	–	59	1.91	0.03
(Ti/Ce)UiO-67	Ce, Ti	H ₂ BPDC	100	100	27.562(1)	–	–	436	1.94	0.21
(Ti/Ce)UiO-66@TiO ₂	Ce, Ti	H ₂ BDC	10	9	21.4561(3)	4.5957 (3)	2.9571 (2)	37	1.88	0.02
(Ti/Ce)UiO-66Br@TiO ₂	Ce, Ti	Br-H ₂ BDC	10	7	21.429(4)	4.5936 (3)	2.9568 (2)	21	1.79	0.01
(Ti/Ce)UiO-66-NO ₂ @TiO ₂	Ce, Ti	NO ₂ -H ₂ BDC	10	9	21.502(3)	4.5969 (5)	2.9567 (3)	26	1.84	0.01
(Ti/Ce)UiO-66-NH ₂ @TiO ₂	Ce, Ti	NH ₂ -H ₂ BDC	10	8	21.497(2)	4.5966 (3)	2.9564 (2)	40	1.88	0.02
(Ti/Ce)UiO-66-N@TiO ₂	Ce, Ti	H ₂ PDC	10	7	21.476(3)	4.5952 (3)	2.9566 (2)	17	1.81	0.01
(Ti/Ce)UiO-67@TiO ₂	Ce, Ti	H ₂ BPDC	10	10	27.580(3)	4.5956 (2)	2.9584 (2)	40	1.87	0.02

region at ~ 2.9 eV (Fig. 2b). While the presence of Ce in the (Ti/Ce)UiO-66 MOF structure show the electronic Ce-states at ~ 2.8 eV (Fig. 2c). These results show excellent agreement with our experimental values estimated by DRS (see Section 3.5) with the use of a Tauc plot reported in Table 1, as well as good agreement with the literature data [26–31]. The literature data indicated that the calculated bandgap structure of pristine (Zn)UiO-66 MOF is in the range from 3.9 to 4.6 eV (at the level of DFT) and in the range from 3.8 to 4.1 eV (based on experimentally measured values) [26–31]. While the literature band gap structure of (Ce)UiO-66 MOF is equal to 2.79–3.0 eV [27,28,32]. Periodic calculations on (Ti)UiO-66, (Ce)UiO-66, and (Ti/Ce)UiO-66 MOF show the appearance of a broad band within the original UiO band gap region (Fig. 2d–f). As it is shown at the PODS analysis (Fig. 2b,c), the organic molecules of (Ce)UiO-66 and (Ti/Ce)UiO-66 MOFs mainly contribute to valence band (VB) states, while the conduction band (CB) is mainly contributed to the 4f orbitals of Ce ions. It can be expected that the introduction of Ti⁴⁺ and Ce⁴⁺ ions in the UiO-66 MOF structure leads to a decrease in the band gap value for both (Ce)UiO-66 and (Ti/Ce)UiO-66 MOF structure, which may result in decreased charge transfer energy between the metal and ligand, which is favorable for photocatalytic efficiency. Moreover, these results indicate that the electron density of the metal center in UiO-66 is changed because of the presence of different radius of Ti⁴⁺ and Ce⁴⁺. The highest occupied crystalline orbital (HOCO) for (Ti)UiO-66, (Ce)UiO-66, and (Ti/Ce)UiO-66 MOF structures is shown in Fig. 2d–f, respectively. The HOCO of Ce- and Ti-UiO-66 is delocalized over most of the organic linkers, but in case of bimetallic (Ti/Ce)UiO-66 MOF structures, when Ti⁴⁺ and Ce⁴⁺ ions are introduced the it becomes localized.

3.2. Morphology

The morphological features of the prepared pristine TiO₂, UiO MOFs, and (Ti/Ce)UiO-X@TiO₂ composites were investigated by SEM, and the results are shown in Fig. 1 and S1. SEM images (Fig. 1b and S1) show

that pristine TiO₂ has a flower-like structure that consists of regularly outward-radiating nanorods; in addition, the average diameter distribution was estimated to be approximately 3 μ m, while the diameter and length of each nanorod subunit were approximately 20 nm and 1.5 μ m, respectively. Notably, the network structure was highly porous, as such a well-defined hierarchical structure is useful for future modification [23,33]. Therefore, it was expected that MOF particles would attach to the surface of the TiO₂ nanoflowers. The morphology of the composites (Fig. 1d) shows that during the in situ postsolvothermal process under the mid-reaction conditions (100 °C), a large internal lateral dimension and an array were created (core-shell-like architecture). The UiO MOF nanospheres were distributed quite homogeneously on the surface of TiO₂, indicating that the two components were tightly coupled. The solid continuous porous network was composed of nanometre-sized (50–250 nm) nanoparticles (Fig. 1c), and those that were irregularly arranged tended to agglomerate.

3.3. Crystal structure and surface composition

The powder XRD patterns of pristine TiO₂, (Ce)UiO-X, and (Ti/Ce)UiO-X MOFs, as well hybrid materials, are depicted in Fig. 3 and S2. A series of cerium-organic frameworks (Fig. S2) were well matched with the standard framework (JCPDS no. 4512072 and 7033336) and exhibited reticular structures similar to those of their Zr analogues and crystallized in the space group Fm $\bar{3}$ m [34,35]. The [Ce₆O₄(OH)₄]¹²⁺ clusters were organized in a cubic close-packed arrangement and bridged by twelve different BDC²⁻ molecules to give the structural formula [Ce₆O₄(OH)₄(BDC)₆]. The use of H₂BPDC instead of the H₂BCD ligand resulted in the symmetric expansion of the UiO-66 topology. The introduction of N-heterocyclic linker (H₂PDC) molecules into the UiO-66 structure, as well as H₂BPDC linker substitution, did not modify the crystal construction of UiO-66. The three sharp Bragg reflections observed at $2\theta = 7^\circ$ (111), 8° (002), and 11° (022) correspond to the UiO-66-type MOFs and suggest a high degree of crystallinity. A similar

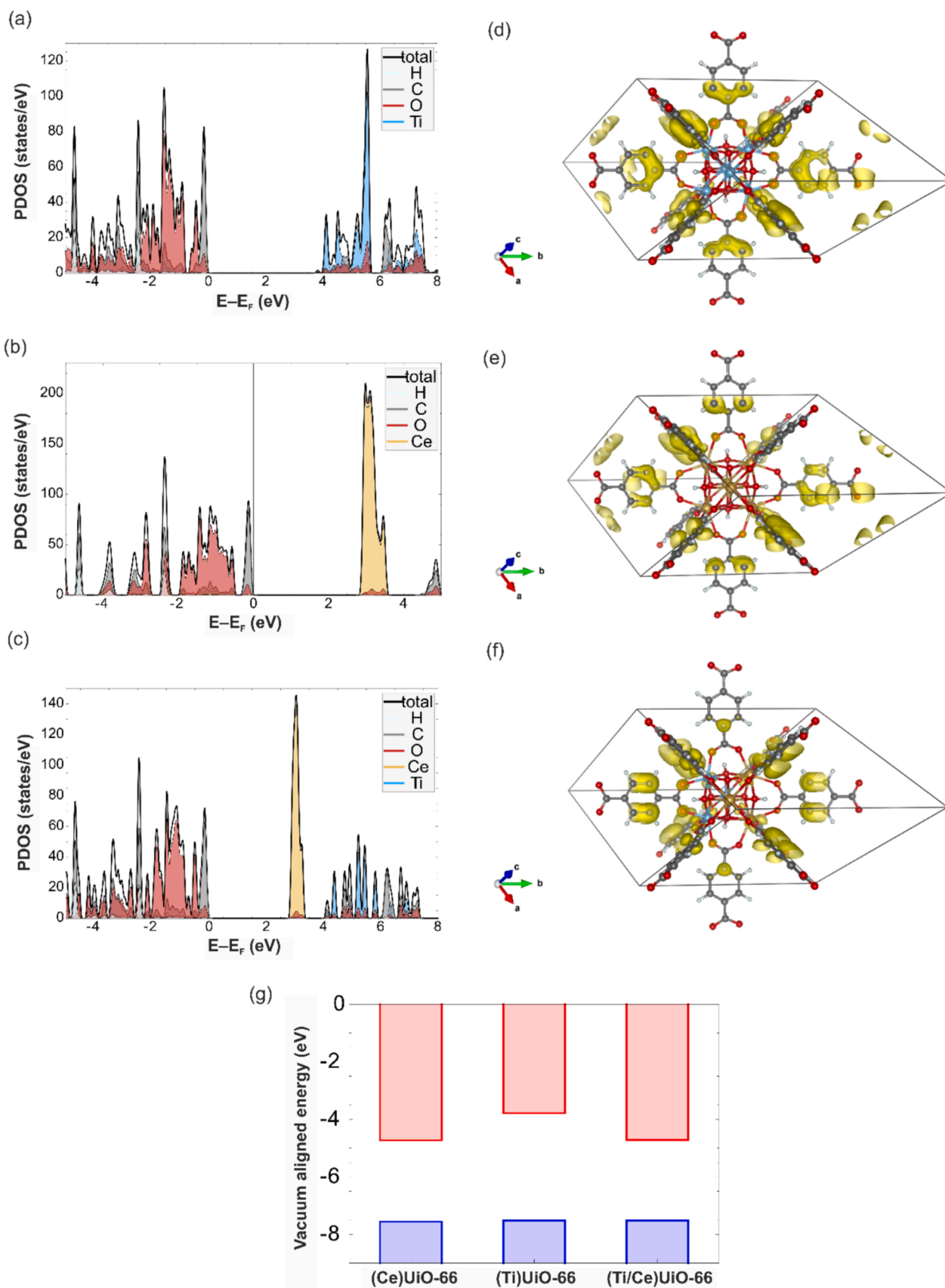


Fig. 2. The calculated PDOS analysis of (a) (Ti)UiO-66, (b) (Ce)UiO-66 and (c) (Ti/Ce)UiO-66 MOF structures, respectively, and (g) the calculated vacuum aligned energy. Electron density of the highest occupied band of (d) (Ti)UiO-66, (e) (Ce)UiO-66, and (f) (Ti/Ce)UiO-66 MOF structures, respectively.

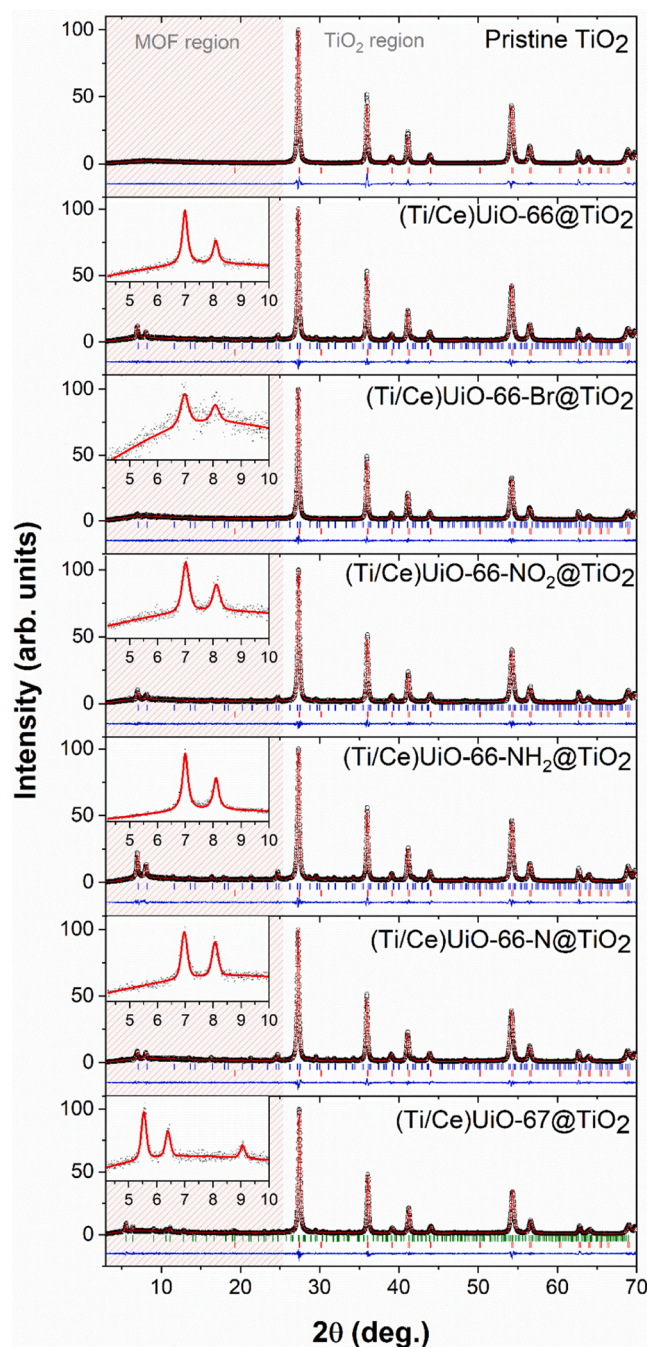


Fig. 3. Powder X-ray diffraction patterns of pristine TiO_2 and $(\text{Ti/Ce})\text{UiO}@-\text{TiO}_2$ composites (inset is the zoomed-in image in the MOF region).

situation is observed for UiO-67 MOF, with reflections found at slightly lower angles of $2\theta = 5^\circ$ (111), 6° (002), and 10° (113), indicating a larger unit cell. Moreover, the typical diffraction pattern of UiO-X MOFs is similar to that of the parent of UiO-66, suggesting that ligand substitution does not change the crystal structure of UiO MOFs [36]. Reflection broadening was observed for the $(\text{Ti/Ce})\text{UiO}-\text{NH}_2$ sample and was probably caused by lattice strain and/or the small size of the nanoparticles. The refined lattice parameters (obtained using the LeBail method) for all studied samples are listed in Table 1. The introduction of Ti did not significantly change the lattice constant. In the case of $(\text{Ce})\text{UiO}-66$ and $(\text{Ti/Ce})\text{UiO}-66$, we observed shrinkage of the crystal lattice from $21.4662(2) \text{ \AA}$ to $21.4179(7) \text{ \AA}$, indicating that heavier Ce was substituted by lighter Ti. Functionalization of the H_2BTC ligand by an

amino group increased the lattice parameters from $21.4179(7) \text{ \AA}$ to $21.4824(1) \text{ \AA}$. The only meaningful increases (compared to the UiO-66 samples) were observed for the $\text{Ce}-\text{UiO}-67$ and $(\text{Ti/Ce})-\text{UiO}-67$ MOFs. For those compounds, the lattice parameter is almost 20% larger, which is due to replacing terephthalic acid with biphenyl-4,4'-dicarboxylic acid. The PXRD pattern of TiO_2 perfectly matches the standard pattern (JCPDS no. 65–0190), for which the characteristic Bragg reflections at $2\theta = 27^\circ, 36^\circ, 39^\circ, 41^\circ, 44^\circ$, and 54° are attributed to the (110), (011), (020), (111), (120), and (121) planes of rutile TiO_2 . The characteristic reflections of both the $(\text{Ti/Ce})\text{UiO}$ MOFs and TiO_2 were observed in the patterns of the $(\text{Ti/Ce})\text{UiO}-\text{X}@-\text{TiO}_2$ hybrid materials, and no additional signs of crystalline impurities formed during the solvothermal process were observed. The observed intensity of the PXRD reflections of UiO MOFs was quite low due to the low amount of surface modification, but it could still be identified, which indicated a two-phase composition. Moreover, the intensities of the UiO MOF phases of the various composite samples were different because the introduction of TiO_2 may have restricted the nucleation and growth of the pure $(\text{Ce})\text{UiO}$ MOFs in various ways. Notably, the presence of characteristic low-angle reflections indicates that $(\text{Ti/Ce})\text{UiO}$ MOF particles were deposited on TiO_2 .

FTIR spectroscopy (Fig. 4 and S3) was employed to demonstrate the features of the surface, chemical bonds, and functional groups of the synthesized samples. The spectra of these Ce- and Ti/Ce-based UiO MOFs show a broad peak in the high wavenumber region assigned to intrinsic $\mu_3\text{-OH}$ groups in the $\text{Ce}_6\text{O}_4(\text{OH})_4$ MOF SBU clusters ($3666\text{--}3635 \text{ cm}^{-1}$), which may be partially overshadowed by the OH groups ($3400\text{--}2800 \text{ cm}^{-1}$) of adsorbed solvent molecules (supposedly DMF and water) interacting via mutual H-bonds within the pores of the MOF [37–39]. Peaks attributed to the anti-symmetric ($1590\text{--}1550 \text{ cm}^{-1}$) and symmetric ($1390\text{--}1370 \text{ cm}^{-1}$) stretching of the carboxylate groups are present in the spectra of all the MOF compounds. In general, similar characteristic bands were observed for all X- H_2BDC , H_2PDC , and H_2BPDC linkers. The $\nu(\text{C}=\text{O})$ and $\nu(\text{C}-\text{O})$ modes of the acid disappeared from the MOF spectra and were replaced by the ν_{as} and ν_{s} modes of the COO^- groups, indicating that complexation took place [40]. The gap between these two bands ($\Delta\nu = 170 \pm 10 \text{ cm}^{-1}$) indicates the connection of the COO^- group of the linker with cerium metal through the bidentate mode of linking [41]. Finally, intramolecular vibrations were recorded in the low-frequency region. It was observed that the incorporation of a specific functional group into the BDC-based MOF structure led to the emergence of new characteristic spectral features in the spectrum of the material. These were the (1) C-X functional group modes, (2) vibration bands of the X moiety, and (3) changed spectral bands of the linker or inorganic node [39]. Nonetheless, in many cases, different modes can be observed at very similar frequencies. For example, in the spectrum of UiO-66-Br, the main bands corresponding to the C-Br bond vibration were observed at $\sim 715 \text{ cm}^{-1}$ [42]. In the spectrum of UiO-66- NO_2 , two additional bands, $\nu_{\text{s}}(\text{NO}_2)$ and $\nu_{\text{as}}(\text{NO}_2)$, were observed; the first band was centred at 1536 cm^{-1} , and the second, partially overshadowed by a strong band attributed to a carboxylate mode, appeared as a shoulder at $\sim 1356 \text{ cm}^{-1}$. The $\nu(\text{C}-\text{N})$ band at 872 cm^{-1} was also recorded. In the spectrum of the amino-tagged sample UiO-66- NH_2 , the primary aromatic amino group displayed two medium absorptions, one at 3465 cm^{-1} and the other at 3346 cm^{-1} , assigned to the asymmetric and symmetric $\nu(\text{N}-\text{H})$ stretching modes, respectively. Among these features, two other characteristic bands of the amino group could be distinguished: the medium $\nu(\text{N}-\text{H})$ bending (scissoring) vibration at 1624 cm^{-1} and the strong $\nu(\text{C}-\text{N})$ stretching distinctive of aromatic amines at 1335 cm^{-1} [42]. In turn, the 2,5-disubstituted pyridine stretching peaks were located at 825 cm^{-1} and 758 cm^{-1} and were present in the spectrum of the UiO-66-N MOFs. A detailed investigation of the UiO-67 framework showed a spectrum very similar to that of the UiO-66 material [43]. Moreover, the use of the longer BPDC linker resulted in an extra peak at 1176 cm^{-1} , which was assigned to a collective mode of the linker and was in excellent agreement with the

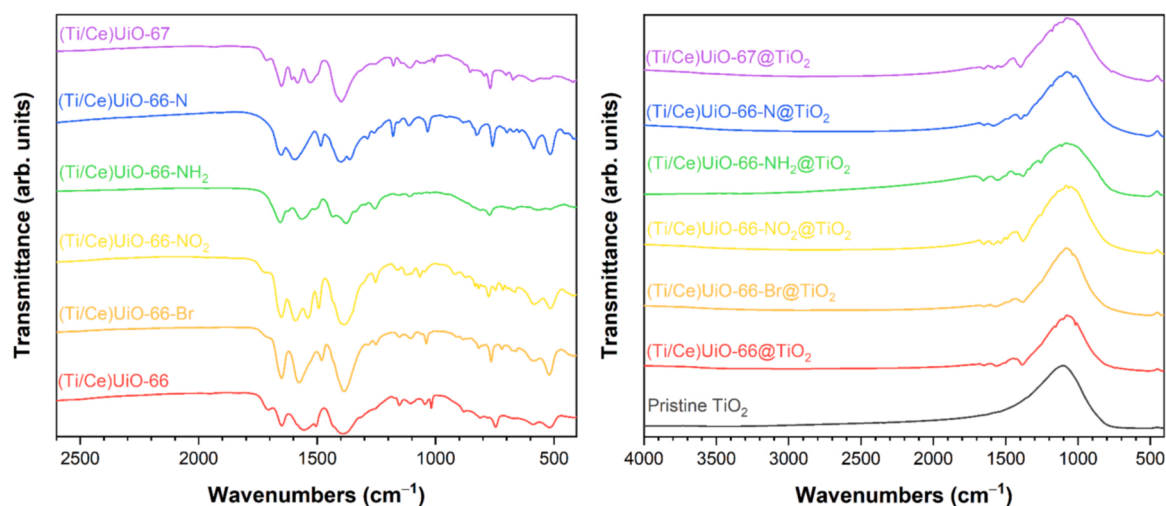


Fig. 4. Fourier transform infrared spectra of (Ti/Ce)UiO-X MOFs (right) and (Ti/Ce)UiO@TiO₂ composites (left).

calculated theoretical value of 1180 cm⁻¹ [31]. The band at 671 cm⁻¹ was linked to the interactions of Ce³⁺ with the carbon moiety (COOH) in the BPDC ligand [39,44]. Pristine TiO₂ exhibits a strong, extensive adsorption peak at 500–700 cm⁻¹, which was attributed to ν(Ti–O) stretching [45]. After a combination of TiO₂ with UiO MOFs, the intensity of the MOF bands was considerably reduced and overlapped with the peak for TiO₂, demonstrating the construction of the anticipated composite among these two materials.

The chemical composition at the surface layer of pristine TiO₂, UiO MOFs, and the (Ti/Ce)UiO-X@TiO₂ composites was evaluated by XPS. Both the elemental composition and the chemical character of the elements identified after analysis of the high-resolution (HR) XPS spectra are summarized in Table 2. An example set of HR spectra, representative of all composites, is presented in Fig. 4 and shows the spectra of the (Ce)UiO, (Ti/Ce)UiO and (Ti/Ce)UiO@TiO₂ samples. Below, the corresponding set of HR spectra is presented for the (Ti/Ce)UiO-66-NH₂ sample, which exhibited the highest efficiency in the photocatalytic experiments. The chemical characteristics of the elements identified after deconvolution of their HR spectra [46] are described in Fig. 5. Moreover, the relative contributions of the chemical states of cerium and titanium, evaluated from the Ce 3d and Ti 2p spectra, respectively, are presented in separate columns of Table 2. The original high-resolution

Ce 3d and Ti 2p XPS spectra for pristine TiO₂ and all (Ti/Ce)UiO@-TiO₂ composites investigated are shown in Fig. S4. Two chemical states of titanium (identified as Ti⁴⁺ and Ti³⁺) were deconvoluted in the Ti 2p spectra recorded for all (Ti/Ce)UiO-X@TiO₂ hybrid materials (the BEs of the Ti 2p_{3/2} peaks were approximately 458.6 eV and 456.6 eV, respectively). Deconvolution of the Ce 3d spectra for mixed Ce⁴⁺ and Ce³⁺ oxide species is very complex and has been widely discussed [47]. To gain additional insight into the relative contribution of both Ce species, we used the same fitting model for all samples. For this purpose, we applied the work of Romeo et al. [48] with that of Pfau and Schierbaum [49], where the Ce 3d spectrum was separated into five doublets, corresponding to the spin–orbit split 3d_{5/2} and 3d_{3/2} signals. The spin–orbit separation was 18.5 eV for peaks related to Ce⁴⁺ and 18.2–18.4 eV for Ce³⁺, and the intensity ratio between the 3d_{5/2} and 3d_{3/2} peaks was set to 1.5. Additionally, we used the parameters of the peak fitting of the Ce 3d spectra evaluated for separate CeO₂ and Ce₂O₃ standards [47,49], where the intensity ratio of the peaks belonging to the same Ce 3d component were constant (please see the A/C=0.54 and B/D=1.56 ratios for the Ce 3d_{5/2} signals referring to the Ce³⁺ and Ce⁴⁺ components, respectively, in Fig. 4). It is expected that the application of this model fitting will provide a more comparative method for Ce 3d spectral analysis. The Ce 3d_{5/2} peaks at BEs of 881.6 ± 0.2 eV and 885.7

Table 2

Elemental composition (in atomic %) of the surface layer of TiO₂ and Ti/Ce frameworks with UiO architecture-modified TiO₂ compositions, evaluated by XPS analysis. The chemical characteristics of cerium and titanium evaluated from Ce 3d and Ti 2p spectra, respectively, are presented in separate columns.

Sample label	Elemental composition (atomic %.)						Ti/Ce	Ce 3d fraction (%)		Ce ³⁺ /Ce ⁴⁺	Ti 2p _{3/2} fraction (%)	
	Ce	Ti	O	C	N	Br		Ce ³⁺	Ce ⁴⁺		Ti ⁴⁺ 458.6 ± 0.2 eV	Ti ³⁺ 456.8 ± 0.3 eV
TiO ₂ (rutile)	–	24.91	66.71	8.38	–	–	–	–	–	–	93.41	6.59
(Ce)UiO-66	5.59	–	31.00	60.31	3.09	–	–	67.60	32.40	2.09	–	–
(Ce)UiO-66-Br	5.17	–	27.63	57.43	2.15	7.62	–	68.34	31.66	2.16	–	–
(Ce)UiO-66-NO ₂	4.59	–	31.56	57.40	6.46	–	–	67.52	32.48	2.08	–	–
(Ce)UiO-66-NH ₂	3.46	–	24.34	64.72	7.48	–	–	70.69	29.31	2.41	–	–
(Ce)UiO-66-N	5.75	–	36.19	48.33	9.74	–	–	69.60	30.40	2.29	–	–
(Ce)UiO-67	3.32	–	31.59	65.09	–	–	–	56.60	43.40	1.30	–	–
(Ti/Ce)UiO-66	0.95	9.96	37.37	49.02	2.70	–	10.48	74.75	25.25	2.96	89.23	10.77
(Ti/Ce)UiO-66-Br	0.66	4.74	40.23	52.44	1.22	0.72	7.18	59.98	40.02	1.50	99.55	0.45
(Ti/Ce)UiO-66-NO ₂	1.97	9.63	38.72	44.74	4.94	–	4.89	71.60	28.40	2.52	99.43	0.57
(Ti/Ce)UiO-66-NH ₂	1.01	4.62	29.05	58.62	6.71	–	4.57	80.43	19.57	4.11	95.62	4.38
(Ti/Ce)UiO-66-N	3.09	4.54	32.58	53.99	5.81	–	1.47	77.08	22.92	3.36	98.76	1.24
(Ti/Ce)UiO-67	0.39	6.66	28.66	62.13	2.16	–	17.08	71.25	28.75	2.48	95.51	4.49
(Ti/Ce)UiO-66@TiO ₂	2.98	8.43	38.28	47.53	2.79	–	2.83	69.48	30.52	2.28	97.82	2.18
(Ti/Ce)UiO-66-Br@TiO ₂	2.16	10.23	38.73	43.19	2.77	2.92	4.74	77.58	22.42	3.46	97.54	2.46
(Ti/Ce)UiO-66-NO ₂ @TiO ₂	2.42	8.00	38.11	45.99	5.50	–	3.31	77.10	22.90	3.36	99.23	0.77
(Ti/Ce)UiO-66-NH ₂ @TiO ₂	2.25	8.03	35.69	49.28	4.74	–	3.57	78.49	21.51	3.65	99.32	0.68
(Ti/Ce)UiO-66-N@TiO ₂	2.30	12.87	45.68	34.75	4.41	–	5.60	76.55	23.45	3.26	98.99	1.01
(Ti/Ce)UiO-67@TiO ₂	2.61	7.94	36.71	50.26	2.48	–	3.04	75.92	24.08	3.15	98.16	1.84

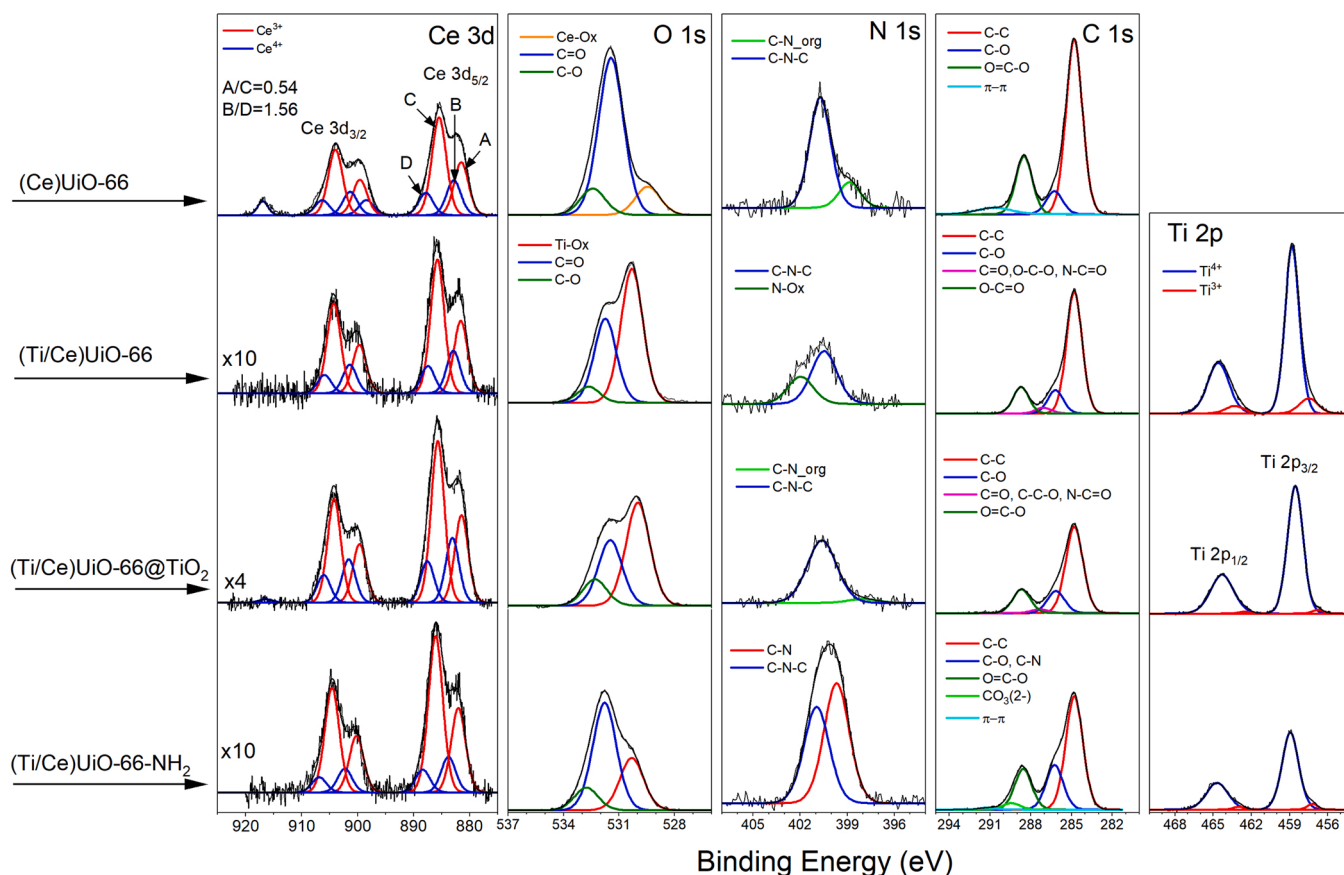


Fig. 5. High-resolution Ce 3d, O 1 s, N 1 s, C 1 s, and Ti 2p XPS spectra recorded for the (Ce)UiO, (Ti/Ce)UiO, and (Ti/Ce)UiO@TiO₂ composites. Below the high resolution, XPS spectra of elements detected at the surface region of the (Ti/Ce)UiO-66-NH₂ composite are presented.

± 0.2 eV were related to the Ce³⁺ species, while the corresponding peaks at 883.1 ± 0.4 eV, 887.8 ± 0.3 eV and 898.1 ± 0.3 eV were assigned to the Ce⁴⁺ species [x-5, x-6]. All deconvoluted peaks were used to determine the relative contributions of the Ce³⁺ and Ce⁴⁺ states (Table 2). Following this model of analysis, we observed the highest amount of Ce³⁺ species in the (Ti/Ce)UiO-66-NH₂ sample among all the composites. This sample also exhibits a high amount of Ti³⁺ states at the surface. It is also important to note that the amounts of Ce and Ti at the surface of the (Ti/Ce)UiO-X hybrid materials were different (see the Ti/Ce ratios in Table 2) and depended on the linker MOFs. However, the number of Ce³⁺ species at the surface of the (Ce)UiO-X samples significantly increased in the samples synthesized with TiO₂ (Table 2).

Based on the above experimental results (supported by PXRD, FTIR, and XPS measurements) and literature data [25], a mechanism for UiO MOF deposition on TiO₂ can be proposed (illustrated in Fig. 1a). During H₂BDC deprotonation, adsorption on rutile TiO₂ forms bridging hydroxyl and bidentate terephthalate species on both surfaces, creating the initial surface precursor for MOF growth. This is followed by a reaction between the fast coordination between the cerium aqua complex [Ce₆O₄(OH)₄]¹²⁺ and the ligand anion that enriches the interface with the metal complex-linker species at a supersaturated concentration that promotes further MOF crystal growth. In summary, the step-by-step deposition of (Ce)UiO MOF on the TiO₂ surface involves the following steps: (1) dissociation of H₂BDC (protonated ligand), (2) nucleation, in which Ce(IV) species rapidly adsorb on the TiO₂-COO⁻ surface, (3) ligand exchange between coordinated nitrate ammonium and ligand acid, (4) (Ce)UiO structure formation, and (5) continuous film growth with (Ce)UiO crystallite coalescence to form a dense film [25].

3.4. TG-DTA and BET surface area measurements

Thermogravimetry-differential thermal analysis (TG-DTA) was carried out for all materials to monitor the thermal stability. As shown in Fig. S5, only ~1% weight loss in the range of 30–800 °C was observed for pristine TiO₂, which is related to the desorption of surface water by evaporation. The TG analysis results of the (Ce)UiO and (Ce/Ti)UiO MOF samples presented three weight loss steps: the first weight loss peak at 50–150 °C can be explained by dehydration, the second peak at 150–350 °C can be attributed to desorption of solvent molecules adsorbed in the pores, and the third peak at 350–800 °C can be assigned to the framework collapse of the MOFs. (Ce)UiO-66-Bi is the most stable of the functionalized Ce-MOFs. In general, (Ti/Ce)UiO MOFs show a decrease in the final residue mass relative to the parent (Ce)UiO frameworks, consistent with the expectations for the exchange of lighter elements. The chemical structure changes of the selected (Ce)- and (Ti/Ce)UiO-66 samples were monitored during thermal degradation by real-time FTIR (Fig. S6). Some variations could be observed with increasing temperature. The bimetallic MOFs exhibited a slower weight loss, which mainly involved the release of CO₂ (2358 cm⁻¹). Additionally, the TG/FTIR spectra of Ce-MOF showed a rapid decrease in relative intensity at 1723 cm⁻¹ (C=O vibrations) and then the complete disappearance of the peak above 330 °C. Moreover, it is worth noting that the nanocomposites possessed higher thermal stability than the (Ti/Ce)UiO MOFs. Overall, TiO₂ and titanium substitution had a synergistic effect on the thermal stability of the (Ce)UiO-66 MOFs. Furthermore, the real contents of the TiO₂ and UiO MOFs in the composites were also quantified by TG. The residual quantity was calculated using the TiO₂-to-MOF mass ratio in the composites by the following equation:

$$\frac{m_{\text{TiO}_2}}{m_{\text{MOF}}} = \frac{(r_{\text{composite}} - r_{\text{MOF}})}{(r_{\text{TiO}_2} - r_{\text{composite}})}$$

where $r_{\text{composite}}$, r_{TiO_2} , and r_{MOF} are the residual mass fractions (%) of the composite, pristine TiO_2 , and (Ti/Ce)UiO MOFs, respectively. As shown in Table 1, the real TiO_2 and UiO MOF contents are approximate to the theoretical values. Liu et al. [50] explained that the real content of ZIF-8 on TiO_2 is lower than theoretical value because in addition to growing on TiO_2 , ZIF-8 also crystallizes in the solution, consuming some of its precursors [50]. Nevertheless, the different values of the composite samples support the assumption of different degrees of UiO-X MOF growth on the TiO_2 surface.

The N_2 adsorption-desorption isotherms of the Ce- and Ti/Ce-UiO-X MOFs and those of the composite materials are depicted in Fig. S7, and a combination of type I isotherms and type IV isotherms with hysteresis loops was observed, indicating their micro- and mesoporous structures [51]. Interestingly, in general, the Ti/Ce-MOFs presented a larger hysteresis loop than the Ce-MOFs. This hysteresis is found primarily in ordered mesoporous materials with a uniform cylindrical pore or ordered three-dimensional pore networks, implying that Ti substitution could induce the generation of more mesopores in the UiO MOF, which could favour the charge transfer and facile diffusion of reactants for enhancing photocatalytic processes. Moreover, this observation could also be attributed to the formation of amorphous or nonporous impurities. The Brunauer–Emmett–Teller (BET) surface area (see Table 1) of the prepared MOF samples fluctuated from 59 to 793 $\text{m}^2\cdot\text{g}^{-1}$ and depended on the type of linker in the UiO MOFs. The functionalized (Ce)UiO MOFs showed a decrease in the specific BET surface area compared with (Ce)UiO-H due to the modification of the substituents, which is consistent with the literature [6]. The (Ti/Ce)-bimetallic MOFs were characterized by a lower surface area than Ce-MOFs, which indicated the partial presence of amorphous Ti retained in the pores of the UiO MOF. Additionally, the TiO_2 surface area was found to be very small (14 $\text{m}^2\cdot\text{g}^{-1}$). As expected, all hybrid composites show a higher BET surface area than pristine TiO_2 ; the MOFs increased the BET surface area to 17–40 $\text{m}^2\cdot\text{g}^{-1}$. The Barrett–Joyner–Halenda (BJH) pore size distribution curves showed that the Ce- and Ti/Ce-MOFs were characterized by microporosity (pores below 2 nm), which indicates that the node is a full linker [52]. In contrast, the hybrid materials exhibited pores of two sizes, micro- and mesopores, which support rapid mass/charge transport and provide

numerous surface-active sites when these hybrids are used as photocatalytic materials.

3.5. Diffuse reflectance spectroscopy (DRS)

The photoresponse range of a semiconductor is an important factor that affects the performance of a photocatalyst. The DRS data of the prepared pristine TiO_2 , (Ce)UiO-X, and (Ti/Ce)UiO-X MOFs, as well as the hybrid materials, were measured in the 250–850 nm range, and the results are shown in Fig. 6. The (Ce)UiO MOF spectra show characteristic broad, intense absorption below 400 nm, which is attributed to the charge transfer transition from O^{2-} (2p) of the BDC linkers to the Ce^{4+} (4f) orbital. Cerium favours ligand-to-metal charge transfer (LMCT) due to the low-lying nature of the empty 4f orbitals of Ce^{4+} , leading to a negative LMCT energy (E_{LMCT}) [53]. Substitution or derivatization of the BDC linker in Ce-based UiO MOFs leads to a bathochromic shift. Although bare Ce-MOFs absorb visible light, a significant increase in absorption up to 800 nm was observed when titanium was incorporated. Ti modification of (Ce)UiO MOFs resulted in a colour change from white–yellowish to beige or brown depending on the MOFs. Wang et al. [9] and Zhang et al. [8] reported that Ti substitution of the UiO-66 MOF subfamily could extend the lifetime of excited states and change the band structure; they observed that the LUMO level shifted towards the HOMO level, with the HOMO slightly changed, which suggested that the LMCT in the (Ti/Ce)-MOFs should be more efficient than that in the (Ce)-MOFs. Absorption by pristine rutile TiO_2 was confined within the near-ultraviolet region. Benefiting from the incorporation of MOFs, enhanced absorption in the visible light region of hybrid materials was observed with no apparent further redshift, resulting from broadband photon harvesting from the UV to visible range. The bandgaps (BGs) or HOMO-LUMO gaps of the pristine TiO_2 , (Ce)UiO, and (Ti/Ce)UiO MOFs were estimated by using a Tauc plot; they were found to be 2.98 eV for TiO_2 , 2.69–2.98 eV for (Ce)UiO, and 2.39–2.93 eV for the (Ti/Ce)UiO MOFs (Table 1). The functionalization of the terephthalate linker in the UiO MOF reduced the HOMO-LUMO gap (except that of the MOF containing NO_2 groups), leading to their expanded light-absorption capability. Furthermore, the metal-exchange samples gave rise to a shoulder peak centred at lower energies, suggesting that a charge-transfer band appeared.

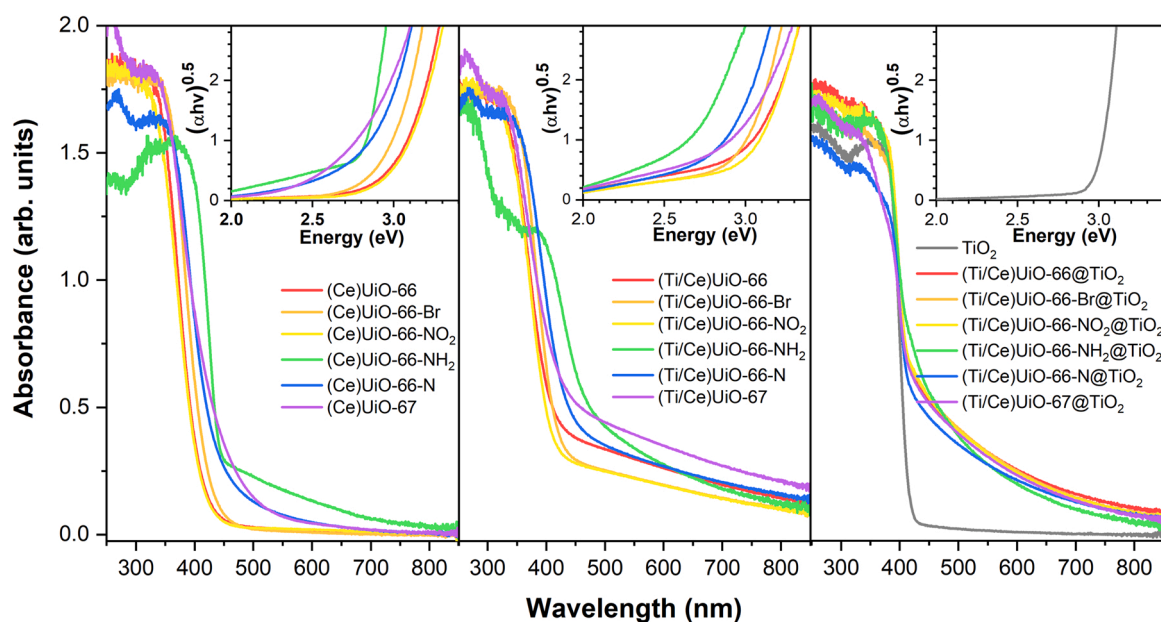


Fig. 6. Ultraviolet–visible absorption spectra of the (Ce)UiO and (Ti/Ce)UiO MOFs, pristine TiO_2 , and (Ti/Ce)UiO@ TiO_2 composites. Inset graphs show the Kubelka–Munk transformation of the (Ce)UiO and (Ti/Ce)UiO MOFs and pristine TiO_2 .

3.6. Photocatalytic activity

The photocatalytic properties of the obtained materials were investigated using various photocatalytic reactions: chromium reduction, hydrogen production, and phenol degradation in the aqueous phase under different ranges of UV–Vis and visible light irradiation. The preliminary studies included control tests, such as photolysis tests (without photocatalysts) and dark tests (without light irradiation).

It has been reported that the photoactivities of functionalized UiO MOFs are correlated with the electronic nature of their linker substituents in photocatalytic oxidation and/or reduction. In the present study, the photoreduction reaction of Cr(VI) was applied for the first time as a model reduction reaction to verify the type of substitution of the linker and its influence on the photoreduction of (Ce)- and (Ti/Ce) UiO-X MOFs. These results will enable MOF selection for further hydrogen production studies. Furthermore, metal-organic frameworks were characterized by exceptional surface areas and high porosity, which may lead to high Cr(VI) adsorption; thus, the sorption test in the dark and the dose of MOFs were optimized. Adsorption-desorption equilibrium on the MOF surfaces was reached after 40 min (thereafter, the adsorption capacity remained almost constant for all the MOF samples), and the optimal dose was 1 g·L⁻¹. Visible light irradiation ($\lambda > 420$ nm) was selected as the low-energy wavelength for the photoreduction of Cr(VI). As the DRS data showed (Fig. 6), all types of MOFs exhibited comparable light absorption ability; thus, the efficiency of Cr(VI) reduction to Cr(III) depended slightly on the absorption of light and strongly on another factor. The relatively low number of electrons photogenerated during irradiation with visible light, in contrast to UV irradiation, led to the observed synergistic effects of the Ce⁴⁺/Ce³⁺ and

Ti⁴⁺/Ti³⁺ redox mediators and the type of linker substituent -X. The results of Cr(VI) photoreduction in the presence of (Ce)- and (Ti/Ce)-UiO-X MOFs under visible light are shown in Fig. S8 and Table 3. The Cr₂O₇²⁻ ions (pH 3) were stable in the selected range of irradiation during the experiments. The photoreduction properties of the obtained materials with Ce⁴⁺/Ce³⁺ followed the order (Ce)UiO-X: -NH₂ > biphenyl > -N- > -H = -Br > -NO₂. Introduction of NO₂⁻ into the linker inhibited Cr(VI) photoreduction, and the presence of Br⁻ had no effects. Based on reported results, unmodified UiO-type MOFs are characterized by low-efficiency Cr(VI) photoreduction and require complex modification [54–58]. The presented research showed that pure (Ce)UiO-66 degraded Cr(VI) with low efficiency, which could be caused by insufficient photoexcited electron transport; thus, e⁻ were not available in the reaction in Ce⁴⁺/Ce³⁺ nodes due to the effect of UiO geometry. However, the obtained removal efficiency of Cr(VI) in the presence of (Ce)UiO-X MOFs indicated that (i) the elongation linker and (ii) the introduced nitrogen linker substituent with donating effects enhanced the reduction of Cr₂O₇²⁻. Additionally, after the introduction of the second redox mediator Ti⁴⁺/Ti³⁺ into (Ce)UiO-66 MOFs, the sorption capacity of bimetallic MOFs was almost unchanged. The results suggested that the Cr₂O₇²⁻ adsorption capacities of the Ce and Ti/Ce-MOFs were not correlated with the BET measurements (Table 1). However, the bimetallic (Ti/Ce)-MOF samples showed greatly enhanced photocatalytic performance from 42% to 45%, 67–89%, 60–80%, and 40–64% for UiO-66, UiO-66-NH₂, UiO-67, and UiO-66-Br, respectively. In contrast, Cr(VI) photoreduction in the presence of Ag/UiO-66-NH₂ and C₃N₄/UiO-66 was 60% and 55%, respectively [55,57]. Incorporation of Ti into the Ce-MOFs induces oxygen vacancy formation in the Ti-Ce-oxo-cluster and creates Ti³⁺ defects in the lattice (confirmed by

Table 3

Photoactivities of (Ce)- and (Ti/Ce)-UiO-X MOFs and (Ti/Ce)-UiO-X@TiO₂ hybrid photocatalysts under UV–Vis and visible light irradiation.

Sample	Efficiency of Cr(VI) reduction under Vis irradiation after 60 min (%)	Cr(VI) reduction rate under Vis irradiation (μmol·dm ⁻³ ·h ⁻¹)	Amount of H ₂ production after 4 h (μmol·g _{cat} ⁻¹)		H ₂ production rate (μmol·h ⁻¹ ·g _{cat} ⁻¹)		Efficiency of phenol degradation under Vis irradiation after 60 min (%)	Phenol degradation rate under Vis irradiation (μmol·dm ⁻³ ·h ⁻¹)
			UV–Vis	Vis	UV–Vis	Vis		
TiO ₂	–	–	59.4	bld	14.9	bld	5.9	12.5
(Ce)UiO-66	42.2	0.10	50.4	bld	12.6	bld	6.9	14.8
(Ce)UiO-66-Br	40.1	0.26	56.6	bld	14.2	bld	9.4	20.1
(Ce)UiO-66-NO ₂	26.0	0.10	13.8	bld	3.5	bld	11.6	24.7
(Ce)UiO-66-NH ₂	67.4	0.57	75.1	bld	18.8	bld	12.0	25.4
(Ce)UiO-66-N	51.5	0.34	42.1	bld	10.5	bld	10.7	22.8
(Ce)UiO-67	60.3	0.31	70.0	bld	17.5	bld	7.1	14.9
(Ti/Ce)UiO-66	45.1	0.16	245.5	bld	61.4	bld	8.8	18.8
(Ti/Ce)UiO-66-Br	63.9	0.50	294.9	bld	73.7	bld	13.6	28.7
(Ti/Ce)UiO-66-NO ₂	19.3	0.10	41.2	bld	10.3	bld	16.8	35.6
(Ti/Ce)UiO-66-NH ₂	86.1	0.79	347.8	bld	87.0	bld	16.2	34.4
(Ti/Ce)UiO-66-N	49.2	0.39	178.9	bld	44.7	bld	11.7	24.9
(Ti/Ce)UiO-67	80.4	0.49	311.5	bld	77.9	bld	13.5	28.6
(Ti/Ce)UiO-66@TiO ₂	–	–	2268.5	0.1	567.1	0.33	10.5	22.4
(Ti/Ce)UiO-66-Br@TiO ₂	–	–	2152.7	0.4	538.2	1.10	29.8	63.4
(Ti/Ce)UiO-66-NO ₂ @TiO ₂	–	–	1417.7	0.2	354.4	0.47	25.9	55.3
(Ti/Ce)UiO-66-NH ₂ @TiO ₂	–	–	4723.9	1.6	1181.0	4.83	28.3	60.2
(Ti/Ce)UiO-66-N@TiO ₂	–	–	2504.7	0.3	626.2	0.79	22.8	48.4
(Ti/Ce)UiO-67@TiO ₂	–	–	4009.6	0.4	1002.4	1.15	7.9	16.7

– not measured; bld - below limit of detection

XPS analysis), which could trap the electrons and form Ti^{4+} and enhance the photoreduction ability [6,38,39]. Moreover, the defects in the crystal lattice resulted in a higher positive charge of MOFs, which is favourable for $\text{Cr}_2\text{O}_7^{2-}$ ion adsorption due to their electrostatic interactions. Additionally, the highest efficiency was achieved for the (Ti/Ce)UiO-66- NH_2 sample; this high efficiency was attributed to the lone pair of electrons in the amine groups, which can interact with the π^* -orbitals of the benzene ring, leading to the donation of f electrons to the antibonding orbitals [59]. Moreover, the different functional groups and the presence of the second redox mediator $\text{Ti}^{4+}/\text{Ti}^{3+}$ enhanced the $\text{h}^+ - \text{e}^-$ separation and utilization of generated electrons in the photoreduction process (which will be described in Section 3.7). The results of the Cr(VI) removal experiments demonstrated that the electronic effect of the ligand substituent and the presence of redox mediators greatly affected the photoreduction activities of the obtained (Ti/Ce)UiO-X MOFs. Based on the Cr(VI) removal efficiency, (Ti/Ce)UiO-X MOFs showed a higher potential for hydrogen generation.

A key goal of the designed photocatalytic materials is their commercial applicability, including the production of clean fuels; therefore, photocatalytic hydrogen evolution is of great interest. The novel hybrid composites presented in this work were evaluated for photocatalytic hydrogen evolution under UV-Vis and visible light irradiation using triethanolamine (TEOA) as the sacrificial reagent to quench the photo-induced holes, and the results are presented in Table 3 and Fig. 7 and S9. Sacrificial agents (electron donors) play an important role in influencing photocatalytic H_2 production due to their lower oxidation potentials and minimization of charge carrier recombination [60]. The effects of the sacrificial agents (methanol, lactic acid, and TEOA) and the

concentration of the aqueous sacrificial agent solution (5–30 wt%) on the hydrogen production efficiency are presented in the supporting material (Table S4); the findings indicated that 10 wt% TEOA solution is most suitable for the applied process, allowing enhanced H_2 generation efficiency considering the yield-reagent cost relationship. Mass transfer in photocatalytic H_2 production in the context of Fick's law is defined as the migration of mass or chemical species from one position to another (e.g., from high to low concentration). Thus, a higher concentration of sacrificial agent is beneficial for enhancing the mass transfer process; however, at higher concentrations, the diffusion process faces more resistance [3]. Therefore, it is important to establish the optimal electrolyte concentration to promote H_2 reduction. In addition, TEOA displayed the overall best performance among the other sacrificial agents tested (H_2 evolution changed in the sequence: TEOA > methanol > lactic acid). According to the literature data, it can be concluded that TEOA significantly absorbs photogenerated holes, improves the dispersion of the semiconductor photocatalyst, and acts as a binding ligand to promote the interaction of MOFs with water molecules [61]. No appreciable hydrogen generation was observed in the absence of either the photocatalysts or illumination. Pristine TiO_2 showed a relatively low efficiency of H_2 production, and only $59.4 \mu\text{mol} \cdot \text{g}_{\text{cat}}^{-1}$ was observed after 4 h of exposure to UV-Vis light irradiation. Moreover, no significant hydrogen production was detected when using the pristine (Ce)- and (Ti/Ce)-UiO-X MOF samples (13.8 – 75.1 and 41.2 – $347.8 \mu\text{mol} \cdot \text{g}_{\text{cat}}^{-1}$, respectively) (Figs. S9 and 7a). However, the presence of titanium in UiO MOFs improved the hydrogen evolution (by approximately 2–5 times) resulting from decreasing the HOMO edges (it is more positive), and the reduction potential was closer to that required to reduce

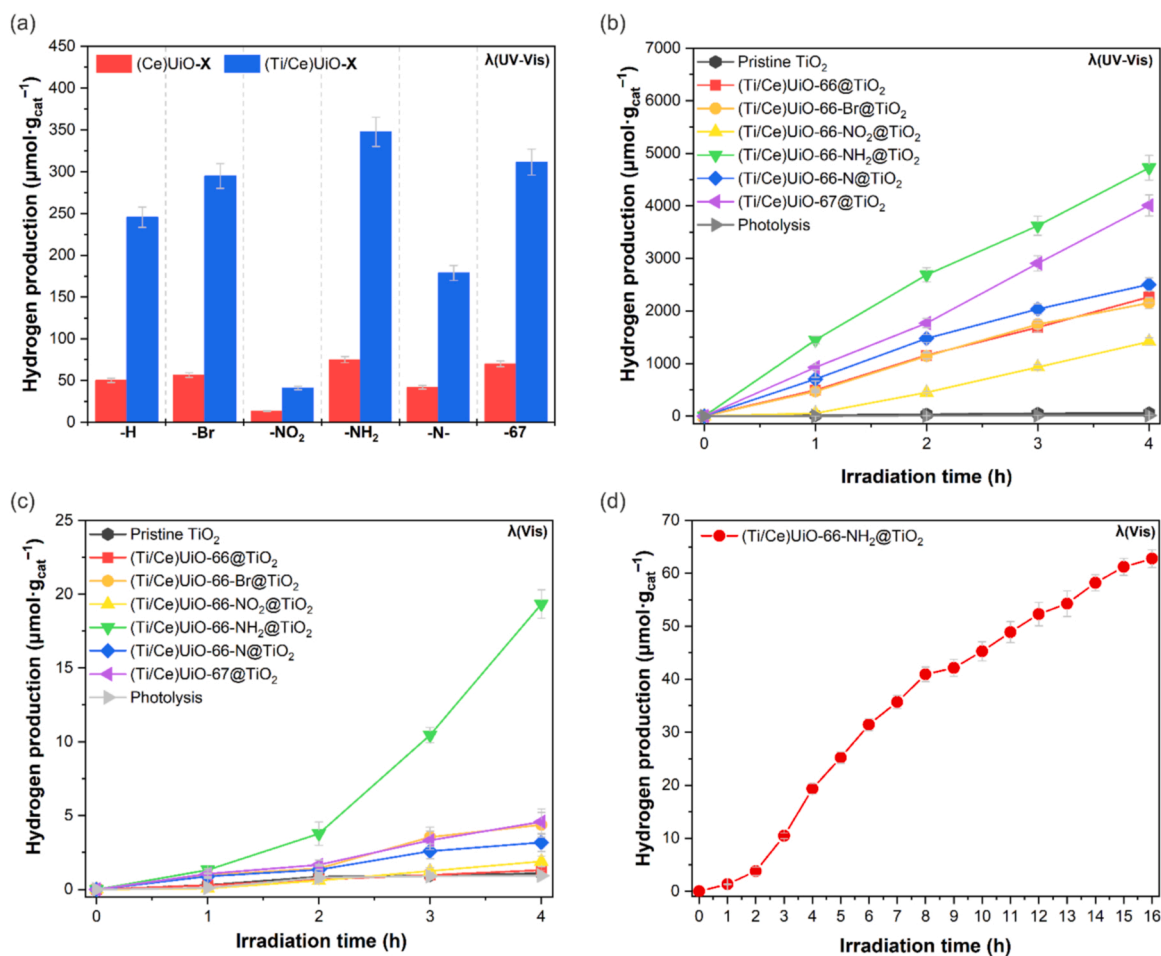


Fig. 7. Hydrogen production in the presence of (a) (Ce)UiO-X, (Ti/Ce)UiO-X MOFs, and (b, c) (Ti/Ce)UiO-X@TiO₂ composite materials under exposure to UV-Vis or visible light irradiation. (d) Long-term hydrogen evolution under visible light irradiation in the presence of the most active sample.

hydrogen. Mao et al. [11] prepared a Au@thiol-UiO66(Zr)@ZnIn₂S₄ composite photocatalyst; both bare thiol-UiO66(Zr) and ZnIn₂S₄ presented lower hydrogen evolution rates (0.9 and 6.4 $\mu\text{mol}\cdot\text{h}^{-1}$, respectively) than the composite materials [11]. Zhang et al. [15] reported that only 7 $\mu\text{mol}\cdot\text{h}^{-1}\cdot\text{g}_{\text{cat}}^{-1}$ hydrogen was produced in the presence of pure MIL-125-NH₂, which was 70 times lower than that of the MIL-125-NH₂@TiO₂ core-shell composite [15]. The less than satisfactory photoactivity of both pristine TiO₂ and pristine MOF samples for H₂ production was mainly ascribed to the fast recombination of photoinduced charge carriers and/or inappropriate VB/LUMO and CB/HOMO edge positions [14]. Therefore, the integration of MOFs with other semiconductors is a promising method for overcoming this problem. The experimental results revealed that the photocatalytic activity of the hybrid material, (Ti/Ce)UiO-X@TiO₂, is significantly better than that of pristine UiO MOFs or pristine TiO₂ under UV-Vis light irradiation (Fig. 7b). This result implies that in situ growth of (Ti/Ce)UiO MOFs onto TiO₂ nanoflowers could noticeably improve the photocatalytic activity for H₂ production. The highest efficiency was achieved for the (Ti/Ce)UiO-66-NH₂-modified TiO₂ sample, which afforded a value of 4724 $\mu\text{mol}\cdot\text{g}_{\text{cat}}^{-1}$ after 4 h of exposure, which is 79 and 14 times higher than that of pristine TiO₂ and pristine (Ti/Ce)UiO-66-NH₂ MOF, respectively. The other composite samples show photoactivity in the range of 1418–4010 $\mu\text{mol}\cdot\text{g}_{\text{cat}}^{-1}$, and the photoactivities changed according to the following order of (Ti/Ce)UiO-X@TiO₂ ligands: -NH₂ > biphenyl > -N- > -H > -Br > -NO₂ > pristine TiO₂. Under visible light (Fig. 7c), the hydrogen production was much lower and was approximately 1.3–19.3 $\mu\text{mol}\cdot\text{g}_{\text{cat}}^{-1}$ after 4 h of photoirradiation. Again, the (Ti/Ce)UiO-66-NH₂@TiO₂ hybrid material resulted in the highest amount of H₂ evolution during visible light irradiation, reaching approximately 19.3 $\mu\text{mol}\cdot\text{g}_{\text{cat}}^{-1}$, which corresponds to a rate equal to 4.8 $\mu\text{mol}\cdot\text{h}^{-1}\cdot\text{g}_{\text{cat}}^{-1}$. Moreover, the most active hybrid materials showed fairly stable photoactivity; the visible light-induced H₂ production efficiency remained consistent even after a prolonged time period of 16 h (Fig. 7d). As reported, efficient mass transfer was observed for MOF-based composite materials, which are characterized by increased surface area and porosity [14]. These properties offer active sites for adsorbing sacrificial agents and providing more channels for internal diffusion, as observed in the conducted studies. In addition, it should be noted that the presented composites do not contain noble metals as cocatalysts, which have been widely used for the surface decoration of composite photocatalysts (including MOF-based composites) designed for hydrogen evolution [62–64]. Thus, the prospect and importance of producing highly photoactive composites without the use of expensive cocatalysts has been proven.

To evaluate the use of the obtained composite photocatalysts as

potential multitasking materials for various other applications (including the oxidation of organic pollutants), the photocatalytic activities of pristine TiO₂, (Ce)UiO, and (Ti/Ce)UiO MOFs and composites were assessed using a model phenol degradation reaction in an aqueous phase under visible light irradiation (Table 3 and Fig. 8a). As expected, pristine TiO₂, (Ce)UiO, and (Ti/Ce)UiO MOFs showed no noticeable photoactivity (5–17%), and the differences in sample performance were not statistically significant. The (Ti/Ce)UiO-X@TiO₂ hybrid nanocomposites with different substituents or derivatives depicted higher activity and changed in the order (Ti/Ce)UiO-X@TiO₂: -Br > -NH₂ > -NO₂ > -N- > -H > biphenyl > pristine TiO₂. The photocatalysts (Ti/Ce)UiO-66-Br@TiO₂ and (Ti/Ce)UiO-66-NH₂@TiO₂ exhibited the highest phenol degradation efficiency, reaching 29.8% and 28.3% when irradiated with visible light for 60 min, respectively. Moreover, the samples exhibited maximum degradation rates of 63.4 and 60.2 $\mu\text{mol}\cdot\text{dm}^{-3}\cdot\text{h}^{-1}$, which were 5.1 and 4.8 times higher than those of pristine TiO₂. Prolonging the exposure time to 6 h resulted in 94.2% effective removal of phenol under visible light irradiation in the presence of (Ti/Ce)UiO-Br@TiO₂. The formation of intermediate organic compounds during phenol photodegradation was examined using HPLC, and the obtained results are presented in Table S5. Generally, the main products of phenol oxidation were catechol, hydroquinone, and benzoquinone. The concentration of the formed intermediates increased with an increase in the efficiency of phenol photodegradation. The number of intermediates generated after 60 min of visible light irradiation was the highest for the process performed in the presence of (Ti/Ce)UiO-Br@TiO₂, which was the most active sample. Moreover, the concentrations of catechol and benzoquinone increased during the process, whereas the concentration of hydroquinone began to decrease after 40 min of visible light exposure (Fig. S10). As shown in Fig. 8b, the sample showed a modest decrease (5%) in photoactivity when reused. Generally, the increase in photocatalytic activity is attributed to electronegative inductive effects (the presence of electron-withdrawing groups), thus increasing the Lewis acidity of the solid material as the inductive effect of the substituent in the aromatic ring increases [65]. This trend excludes the NH₂-tagged sample, which was the second-most active sample. This demonstrated that the light absorption capability, chemical stability, and suitable band edge positions of narrow band gaps are not the only decisive factors to enhance the phenol photodegradation efficiency. The structure of the best sample prior to and after (Ti/Ce)UiO-NH₂@TiO₂ (both phenol degradation and hydrogen generation) was examined by PXRD (Fig. S11). No phase changes or structural damage occurred during the phenol photodegradation reaction. The results suggest that the change in photoactivity of the composite photocatalyst was due to volume transformations rather than

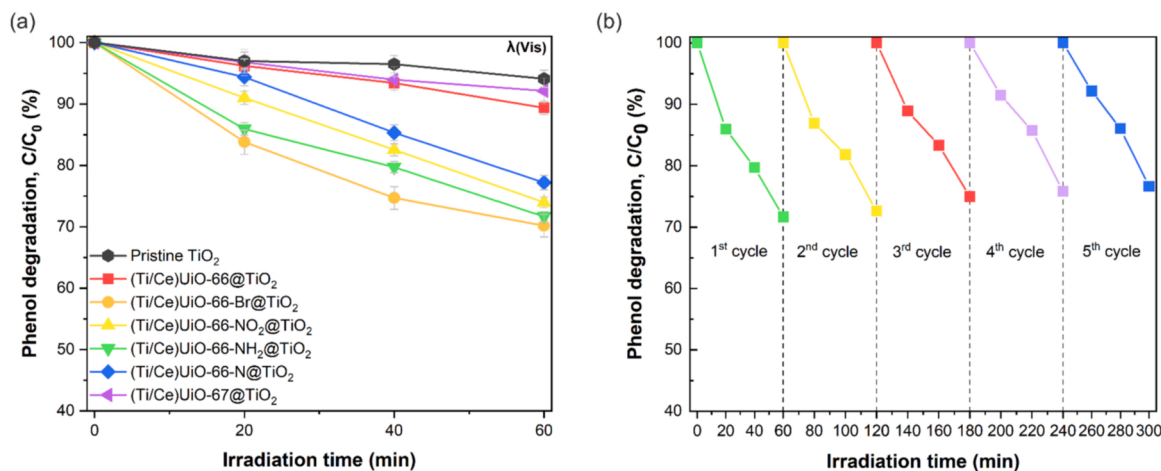


Fig. 8. (a) Efficiency of phenol degradation under visible light irradiation in the presence of pristine TiO₂ and (Ti/Ce)UiO-X@TiO₂ composite materials. (b) Photostability during five cycles of most active sample use.

surface transformations. This evidence is different from that of the sample after the hydrogen generation reaction, where it was observed in the PXRD pattern that the rutile phase remained unchanged, while the peaks originating from the MOFs vanished. The observed surface amorphization is very often described in the literature and can be explained by the photogeneration of oxygen vacancies and the resulting dissociation of water at these defect sites. Zhang et al. [66] observed that when titania is exposed to light and water vapour, the initially crystalline surface transforms into a stable and heavily hydroxylated amorphous phase with a thickness ranging from one layer to multiple monolayers. Moreover, they concluded that this disordered layer would be present on the surface under the reaction conditions required for the photocatalytic splitting of water [66]. However, it is also possible that the metal-organic framework could have been damaged by radiation or active species generated during the reaction. The structure of the (Ti/Ce) UiO-66-NH₂ MOF-coated TiO₂ nanoflower after hydrogen generation was investigated via SEM; no significant changes in MOF morphology were observed. Therefore, additional tests were performed to determine the stability of the stability under irradiation in the absence of TEOA (pure water), and the photodegradation of phenol in the presence of the TEOA sacrificial agent (20 mg·L⁻¹ aqueous solution of phenol with 10% TEOA). XRD analysis showed that the sample was stable under all the above conditions. Moreover, it still exhibited photocatalytic activity in phenol degradation. Based on these observations, the structural changes after hydrogen production noted in the PXRD pattern are probably due to both partial decomposition of the (Ti/Ce)UiO-66-NH₂ MOF and surface amorphization.

Different types of materials (metal-organic frameworks compared to inorganic titanium dioxide) are characterized by different optical properties, and thus, operational parameters such as optimal photocatalyst loading should be investigated. Therefore, the optical properties of pristine TiO₂ and hybrid materials (absorption and scattering coefficients, optical thickness) were determined. The optical parameters of the photocatalyst suspension in water (0.5, 0.75, 1, 1.25 and 1.5 g·L⁻¹) were averaged over the UV (350–400 nm) and visible (400–750 nm) spectral ranges to simplify the modelling methodology, according to a previously described procedure [67,68], and the absorption-scattering parameters were calculated based on the equations presented in Grčić et al. [69]. Pristine TiO₂ interacts with light significantly only in the UV region, while (Ti/Ce)UiO-X@TiO₂ composites can absorb a large amount of UV and visible radiation (see Fig. 6). The optical parameters were fitted from the experimental averaged results of pristine TiO₂ and (Ti/Ce)UiO@TiO₂ hybrid samples and are reported in Table S6. Generally, the particles of (Ti/Ce)UiO@TiO₂ in aqueous suspension were found to have a significantly high degree of scattering. The specific scattering coefficient of the (Ti/Ce)UiO-66-N@TiO₂ composite was 1.7 times higher than the corresponding values for pristine TiO₂ in the 350–400 nm range. Moreover, the scattering coefficient of composite samples under the UV region changed in the order of (Ti/Ce)UiO-X@TiO₂: -N- > -NH₂ > biphenyl > -NO₂ > pristine TiO₂ > -Br > -H. The high scattering coefficient may indicate that a large proportion of the supplied photons do not participate in the photoactivation of TiO₂ unless multiple scattering can occur. The scattering phenomena also depend on the particle size, porosity and geometry of the particles, among many other factors [70]. Pristine TiO₂ has a flower-like structure, while the composite samples were characterized by a core-shell-like architecture. In addition, the (Ti/Ce)UiO-X@TiO₂ samples possess a high optical coefficient in the visible region and at the same time a low corrected scattering albedo (ω_{corr}), suggesting efficient exploitation of the incident photons [69]. The dependence of the local volumetric rate of photon absorption (LVRPA) on the photocatalyst loading under visible light irradiation is presented in Fig. S12 [71]. The intensity of light supplied to the reaction system was 40 W·m⁻². The samples displayed an almost uniform distribution of LVRPA at all photocatalyst loadings investigated. The maximum LVRPA value was estimated to be 71.5 W·m⁻³ for the (Ti/Ce)UiO-NH₂@TiO₂ composite. From an optical point of view,

the photocatalyst concentration required to reach such a value is 1 g·L⁻¹. In summary, the maximum LVRPA values in the presence of optimum loading decreased in the following order (Ti/Ce)UiO-X@TiO₂: -NH₂ (1 g·L⁻¹) > -Br (1.25 g·L⁻¹) > -N- (1 g·L⁻¹) > -H (1.25 g·L⁻¹) > biphenyl (0.5 g·L⁻¹) > -NO₂ (1 g·L⁻¹). The apparent optical thickness (τ_{app}) in the batch glass photoreactor with a reactor thickness of 0.033 m was equal to 2.8–4.4. The profile gradients were much less sensitive to the photocatalyst dose due to the significantly lower scattering albedos values of the (Ti/Ce)UiO-X@TiO₂ samples, which may favour photon penetration to greater depths in the reactor [68]. The obtained results indicated that the given concentration of photocatalyst (1 g·L⁻¹) for used reactors can be considered optimal. In addition to radiation transport considerations, chemical and physical aspects may also affect the exact optimum photocatalyst concentration for a given substrate. In brief, the obtained negligible differences in optical parameters may indicate that other aspects, such as the position of the CB and VB or the efficiency of charge carrier pair separation, may affect the performance of photocatalytic processes, which is discussed in detail in the next section.

3.7. Elucidation of the mechanism

In general, three principal processes are involved in the photocatalytic reaction: (1) light harvesting, (2) the formation, separation, migration, or recombination of photoinduced electron-hole pairs, and (3) reduction or oxidation achieved by the active species resulting from charge carriers. To determine the possible mechanism of photocatalytic process production over the (Ti/Ce)UiO-X@TiO₂ composite, multistage tests were performed.

Solid-state photoluminescence (PL) spectroscopy measurements were performed to probe the recombination behaviours of the obtained materials. In general, the lower the PL spectral intensity is, the lower the probability of electron-hole recombination, resulting in the higher photocatalytic performance of the photocatalyst [72]. As shown in Fig. S13, under an excitation wavelength of 315 nm, a strong and broad emission at 370–550 nm was observed. The PL intensity decreased in the order of pristine TiO₂ < (Ce)UiO-66 MOFs < (Ti/Ce)UiO-X MOFs < (Ti/Ce)UiO-X@TiO₂ hybrid materials. In particular, (Ti/Ce)UiO-66-NH₂@TiO₂ possessed the highest ability to inhibit e⁻/h⁺ couple recombination (approximately 10 times lower PL intensity than that of pristine TiO₂), which suggests synergy between Ti and Ce in the UiO-66-NH₂ MOF synthesized on TiO₂. Based on the shapes of the spectra, the presence of (Ti/Ce)UiO-X MOFs did not result in new PL phenomena. The obtained results demonstrate that the proposed hybrid material consisting of two semiconductors forming a p-n heterojunction with suitable electronic structures causes effective separation of the photogenerated electrons and holes, driven by the built-in field at the interface, which is favourable for charge separation and utilization yield and improves the photocatalytic performance.

To identify and determine the photogenerated entities, including electrons, holes, and hydroxyl and superoxide radicals, under visible light irradiation ($\lambda > 420$ nm), several types of tests were carried out, including hydroxyl radical generation using TPA, superoxide radical production using NBT and the formation of other reactive species through trapping experiments. The formation of hydroxyl radicals was monitored by spectrometric analysis of photogenerated 2-hydroxyterephthalic acid (a product of the reaction between TPA and hydroxyl radicals); generally, the fluorescence (FL) intensity was proportional to the number of hydroxyl radicals generated at the photocatalyst surface. The test was performed by irradiating the (Ti/Ce)UiO-X MOFs and composite materials in an aqueous TPA solution with visible light, and the results are presented in Fig. 9a. Pristine TiO₂ was used as a reference sample because it is inactive during visible light irradiation. A series of samples based on (Ti/Ce)UiO MOFs showed increases in the intensity of the bands compared to that of pristine TiO₂; however, the results indicated that negligible quantities of hydroxyl radicals were generated (see Fig. S14). The coupling of (Ti/Ce)UiO MOFs and TiO₂ increases the

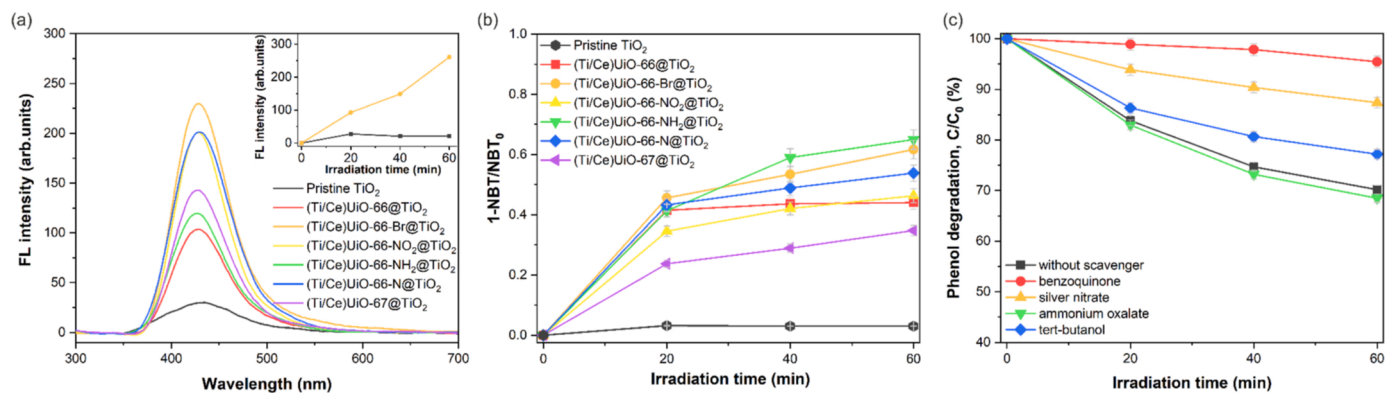


Fig. 9. (a) FL spectra of pristine TiO_2 and $(\text{Ti/Ce})\text{UiO-X@TiO}_2$ after 60 min of visible light irradiation (the insert shows changes in the FL spectra of the TPA solution in the presence of pristine TiO_2 and $(\text{Ti/Ce})\text{UiO-66-Br@TiO}_2$). (b) Changes in the absorption spectra of the solution of NBT under visible light irradiation of pristine TiO_2 and $(\text{Ti/Ce})\text{UiO-X@TiO}_2$ composites. (c) Photocatalytic degradation under visible light irradiation of phenol in the presence of $(\text{Ti/Ce})\text{UiO-66-Br@TiO}_2$ and scavenger.

effectiveness of the generated hydroxyl radicals. The FL spectral intensity increased with increasing exposure time; nevertheless, there was no correlation between the photodegradation efficiency and the amount of $\cdot\text{OH}$. Superoxide radicals were detected by spectrometric analysis of the photoproduct formazan (reaction product of NBT with superoxide radicals). The decrease in the absorption band of NBT is proportional to

the amount of superoxide radicals produced during visible light irradiation of the prepared sample suspension. As shown in Fig. S15, after 40 min of reaction, the quantity of superoxide radicals in the system with $(\text{Ti/Ce})\text{UiO}$ MOFs reached a plateau, in contrast to the quantity in the composite materials; constant increases in the number of photo-generated superoxide radicals (Fig. 9b) using $(\text{Ti/Ce})\text{UiO-X@TiO}_2$

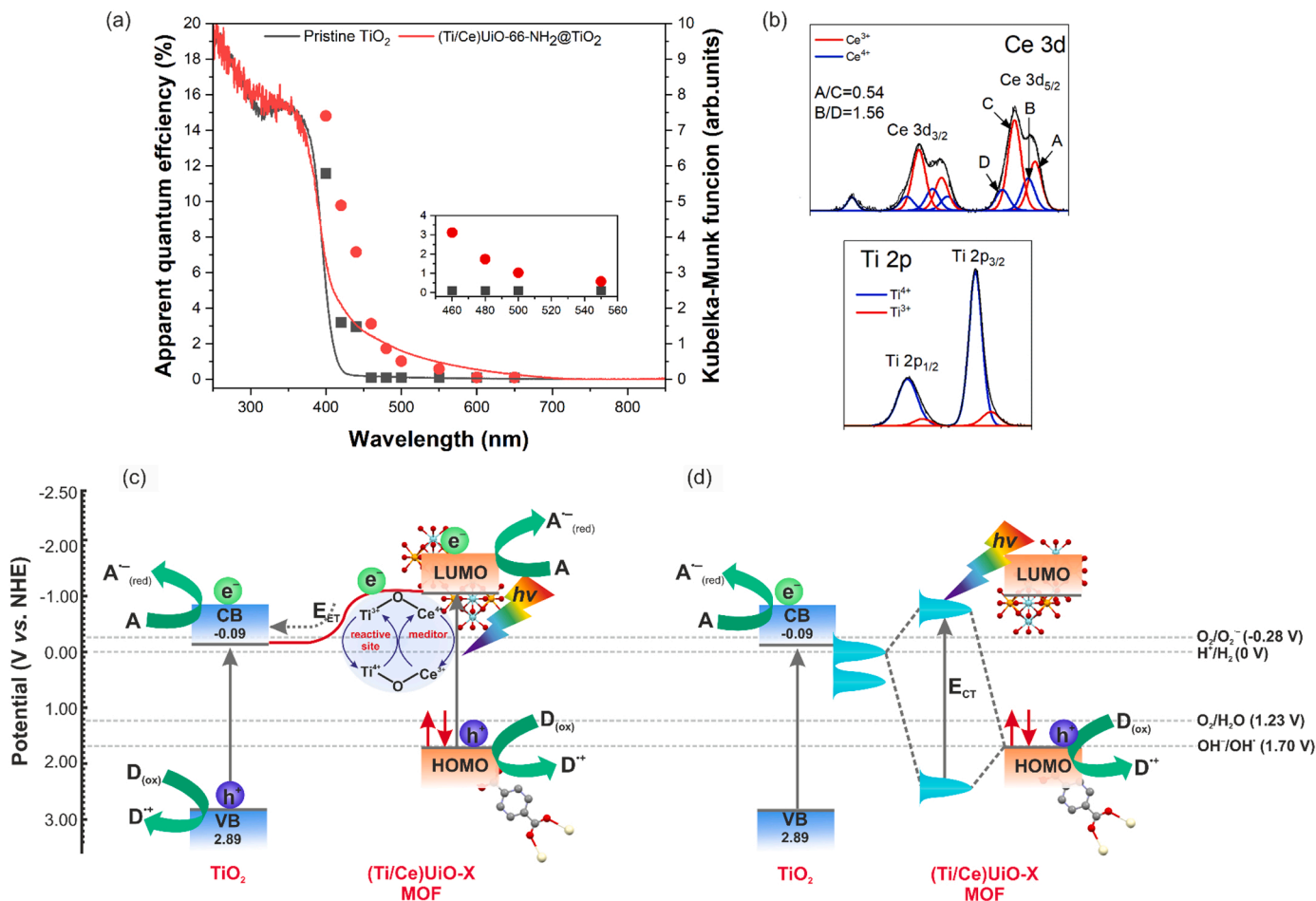


Fig. 10. (a) Action spectral analysis of phenol oxidation with $(\text{Ti/Ce})\text{UiO-66-NH}_2\text{@TiO}_2$ (apparent quantum efficiency: squares and circles; photoabsorption presented as K–M function: lines). (b) High-resolution Ce 3d and Ti 2p XPS spectra presented two chemical states of cerium (identified as Ce^{4+} and Ce^{3+}) and titanium (Ti^{4+} and Ti^{3+}). Proposed mechanism of the excitation of the $(\text{Ti/Ce})\text{UiO-X}$ -modified TiO_2 composite: (c) indirect photosensitization; (d) direct photosensitization (A – electron acceptor, D – donor; the position of HOMO/LUMO levels of $(\text{Ti/Ce})\text{UiO-X}$ MOFs are listed in Table S7).

suggested the good separation of electrons and holes and their positive effect on its photocatalytic activity. The introduction of MOFs on the surface of TiO₂ improved the separation of photogenerated electrons and holes and enabled the generation of O₂^{•−} by the electrons; many additional active sites capable of forming superoxide anion radicals were observed in the NBT experiment. In addition, the main reactive substances formed during the photocatalytic process were identified via active species trapping experiments (Fig. 9c). The photocatalytic degradation of phenol was reduced after the addition of benzoquinone (superoxide radical scavenger) and silver nitrate (electron scavenger); the photodegradation efficiencies decreased from 29.8% to 4.5% and 12.6%, respectively. The photocatalytic efficiency of hydroxyl radicals decreased to only 22.8% in the presence of *tert*-butanol, indicating that •OH radicals were not the main active substances. Moreover, the addition of ammonium oxalate (hole scavenger) increased the efficiency of phenol photodegradation to 31.5%. In summary, superoxide radicals are the main active species produced by (Ti/Ce)UiO MOFs, whereas various active species interact in the composite photocatalytic systems, and the order of their interaction is as follows: O₂^{•−} > e[−] > •OH > h⁺.

To gain insight into the mechanism of the obtained (Ti/Ce)UiO-66-NH₂-modified titania photocatalysts, oxidized phenol was investigated as a function of the excitation wavelength (400, 420, 440, 460, 480, 500, 550, 600, and 650 nm; Fig. 10a). For comparison, the wavelength-dependent apparent quantum efficiency (AQE) determined for pristine TiO₂ is also shown. The (Ti/Ce)UiO-66-NH₂@TiO₂ hybrid composite is highly photoactive in the visible region at 400–550 nm, whereas pristine TiO₂ is active only at 400–440 nm. The AQE values calculated for composite materials are significantly improved compared to those of pristine TiO₂, which correlates well with its photoabsorption properties. The highest AQE in the visible region was observed at 400 nm (14.8%). It can be concluded that under visible light irradiation, (Ti/Ce)UiO MOF acts as an electron donor to initiate photoexcitation of TiO₂.

According to the Mulliken electronegativity theory formulas, the VB and CB levels of TiO₂ were calculated to be 2.80 and −0.18 eV relative to the NHE level, respectively. However, the estimated HOMO/LUMO levels varied depending on the linker used, and the results are shown in Table S7 and Fig. S16. It should be noted that upon Ti incorporation, the LUMO levels shifted towards the HOMO levels. Our research is consistent with the density functional theory (DFT) calculation results of Wu et al. [53]. They found that new filled states form within the original HOMO-LUMO gap of pristine (Ce)UiO-66 after BDC linker functionalization, which pushes the highest occupied orbitals to lowest unoccupied orbitals of the crystal and thereby decreases the gap and the absorption energy (E_{abs}). New filled states tend to appear near the middle of the original HOMO-LUMO gap of pristine (Ce)UiO-66 when the BDC linker is substituted by an electron-donating group (such as NH₂), while substituting the BDC linker with an electron-withdrawing group (for example, NO₂) introduces new filled states located just above the original HOMO of pristine (Ce)UiO-66. Moreover, they found that the occupied node orbitals and empty 4f orbitals remain largely unchanged after linker functionalization; therefore, it is expected that node-localized excitations are still weak [53]. These findings highlight the validity of the additional modifications presented in this paper, which were aimed at increasing the photocatalytic activity for a specific reaction, such as hydrogen generation.

Based on the experimental results, a possible mechanism for the photocatalytic processes (hydrogen production and degradation of contaminants in the aqueous phase) in the presence of (Ti/Ce)UiO@-TiO₂ hybrid materials can be proposed based on the energy levels and charge carrier transfer. In general, there are two different possible mechanisms that could occur at the (Ti/Ce)UiO and TiO₂ interfaces: so-called *photoinduced electron transfer* and *direct optical electron transfer* (Fig. 10). When coupling is weak (Fig. 10c), upon excitation of the (Ti/Ce)UiO-X MOFs, the organic ligand (HOMO level) acts as a photon absorber that can effectively transfer electrons to the metal-oxo cluster (LUMO level), followed by electron injection into the CB of TiO₂. TiO₂,

which can be regarded as a photon acceptor, successfully slows or inhibits electron and hole recombination, thus improving the reaction rate and enhancing the photocatalytic ability [73]. Moreover, according to the Sakata-Hiramoto-Hashimoto model [74], the LUMO level must be located above the CB edge of the n-type semiconductor (see Fig. S16). However, it is well known that the absorption edge can shift after structural changes leading to enhanced conjugation (such as that which causes the BG edge of TiO₂ to bend upwards and that which causes the (Ti/Ce)UiO MOFs to bend downwards). The second mechanism (Fig. 10d) occurs in the case of strong coupling between a semiconductor and molecules, where a new surface coordination species and new energy levels are created [33,75]. Based on the Creutz-Brunschwig-Sutin model [75], a binding orbital is formed between the titanium *d* orbitals of TiO₂ and the molecular levels of the ligand of UiO MOF (HOMO level). Upon excitation of the UiO MOF surface complex, electron transfer is directly promoted to the CB localized at titanium centres at the surface. As a result of the above mechanisms, not only was the separation and transfer process of photogenerated carrier pairs remarkably improved, but the strong redox capability was also preserved in the system. In particular, the resulting energetic positions of the photogenerated charges enabled TEOA oxidation by the holes at the UiO MOF layer while still generating reactive electrons at a relatively negative CB edge of TiO₂, leading to the reduction of H⁺ to H₂. The photogenerated charge couples also allow the production of reactive species that can interact with pollutants such as phenol. The electrons in the LUMO of UiO MOFs are able to reduce molecular oxygen to superoxide radicals, which can lead to the production of hydroxyl radicals when the radicals react with water. However, the holes in the VB of TiO₂ or the HOMO of UiO MOFs can lead to the generation of highly oxidizing hydroxyl radical species, and the holes can directly oxidize pollutants. It is important to note that the calculated band edge positions of CB/LUMO are minimum values, while those of VB/HOMO are maximum values, so although the LUMO of (Ti/Ce)UiO-NO₂ MOF was lower than the redox potential of the superoxide radicals, these radicals can be produced. Furthermore, the presence of electron interactions between the Ce-Ti species results in the formation of two redox mediators, Ce⁴⁺/Ce³⁺ and Ti⁴⁺/Ti³⁺ (Fig. 10b), which promote the generation of more Lewis acid sites on the surface of the photocatalyst. Redox mediators are instrumental in the effective transfer of electrons for high performance photocatalytic processes. Under illumination, O₂ molecules can rapidly and easily diffuse into the UiO MOFs and undergo adsorption on the Ce⁴⁺ or Ti⁴⁺ sites to form O₂^{•−}. More precisely, M⁴⁺ ions absorb photoexcited electrons and are reduced to M³⁺. Then, M³⁺ ions react with O₂ molecules to form O₂^{•−}, while photogenerated holes react with water to produce •OH radicals and produce an oxygen-rich environment around TiO₂. The Hammett constant (σ) [76] for the meta substitution in the aromatic ring was chosen as a representative parameter to correlate with the obtained reaction rates. The Hammett constant represents the effect that different substituents have on the electronic character of a given aromatic system. A relatively good relationship can be observed between the hydrogen production rate when (Ti/Ce)UiO-X@TiO₂ composites are present and the Hammett constant (Fig. 11a). (Ti/Ce)UiO-NH₂@TiO₂ with electron-donating substituents showed higher photocatalytic activity than expected for σ values (−NH₂ > −H > biphenyl > −N− > −Br > −NO₂) [76]. In general, it can be concluded that the hydrogen generation rate was suppressed by electron-withdrawing substituents. This is in contrast to the photodegradation of phenol, where the effect of the substituent is not as significant (Fig. 11b). It is also possible that other factors, such as different adsorption abilities, may contribute to the observed deviation from linearity. The higher phenol photodegradation rate of (Ti/Ce)UiO-Br@TiO₂ compared to that of (Ti/Ce)UiO-NH₂@TiO₂ is mainly attributed to electronegative inductive effects, therefore increasing the Lewis acidity of the solid material as the inductive effect of the substituent in the aromatic ring increases.

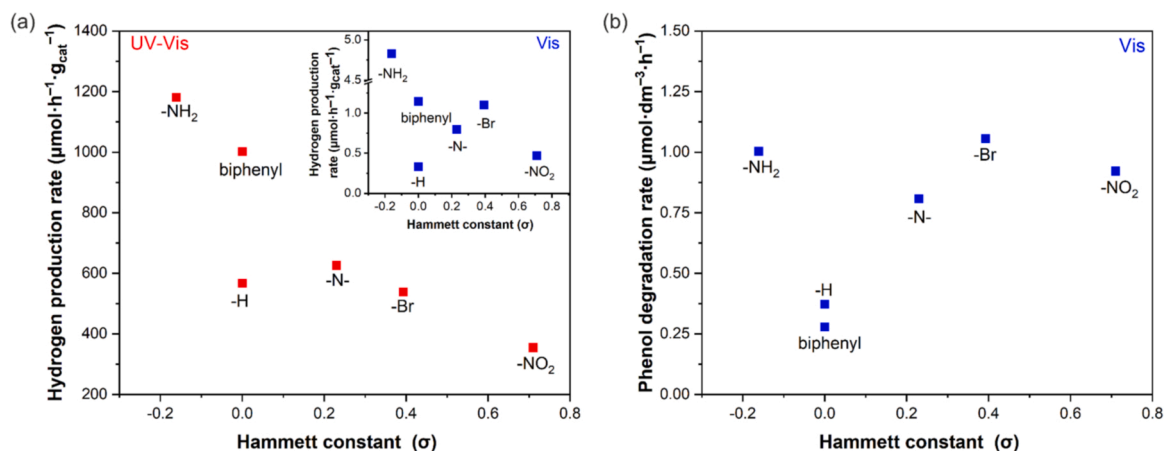


Fig. 11. Correlation between the reaction rate and the Hammett constant (σ) for meta substitution in the aromatic ring: (a) hydrogen production rate and (b) phenol degradation rate in the presence of (Ti/Ce)UiO-X@TiO₂ composites.

4. Conclusions

In this work, it was demonstrated that Ti/Ce-UiO-based MOFs, as efficient electron transfer mediators, work together with TiO₂ to significantly boost photocatalytic hydrogen production and pollutant degradation. DFT simulations showed that Ce- and bimetallic Ti/Ce-MOFs exhibited different charge compensation, and Ti-substitution implies the reduction of HOMO-LUMO gap. Hierarchical flower-like TiO₂ is an excellent matrix for further modification; FTIR and XPS analyses suggested that the adsorption of UiO MOF onto rutile TiO₂ is initiated by H₂BDC ligands, which form bridging hydroxyl and bidentate terephthalate species, which then coordinate with the cerium complex. In the present work, the influence of different parameters, such as the type of ligand (BDC substitution by -Br, -NH₂, -NO₂ or BDC derivatives such as N-heterocyclic and biphenyl groups) and titanium substitution, was investigated to evaluate the photocatalytic behaviour. Chromium reduction screening tests showed that cerium-based UiO MOFs with incorporated Ti exhibited greatly enhanced photocatalytic reduction performance due to the formation of abundant oxygen vacancies in the Ti-Ce-oxo-cluster and Ti³⁺ defects in the lattice (confirmed by XPS analysis). The (Ti/Ce)UiO-66-NH₂ MOF sample had the highest chromium reduction efficiency, reaching 82.6% degradation when irradiated with visible light for 60 min. As expected, the (Ti/Ce)UiO-66-NH₂-modified TiO₂ hybrid material presented the highest photocatalytic hydrogen production efficiencies of 4724 and 19.3 $\mu\text{mol}\cdot\text{g}_{\text{cat}}^{-1}$ after 4 h of UV-Vis and visible light irradiation, which were 79 and 19 times higher than that of pristine TiO₂, respectively. In contrast, the highest phenol degradation efficiency was achieved for the Br-tagged composite sample ((Ti/Ce)UiO-66-Br@TiO₂), which was 29.8% after 60 min of visible light exposure. The enhanced photoactivity of the obtained composite materials compared to that of pristine TiO₂ is attributed to the effective mass transfer resulting from the increased specific surface area and porosity. It was observed that the photocatalytic efficiency depends on the substitution or derivation of UiO-X MOFs. More specifically, the photoactivities of the (Ti/Ce)UiO-X@TiO₂ composite samples changed according to the order -NH₂ > biphenyl > -N- > -H > -Br > -NO₂ > pristine TiO₂ or -Br > -NH₂ > -NO₂ > -N- > -H > biphenyl > pristine TiO₂ for hydrogen production or phenol degradation, respectively. Generally, the increase in hydrogen photocatalytic activity was correlated with the Hammett constant and was mainly attributed to electron-donating groups, whereas the enhanced phenol photodegradation was mainly attributed to electronegative inductive effects (the presence of electron-withdrawing groups). With a few exceptions, the light absorption capability and suitable band edge positions of narrow band gaps are not the only decisive factors that enhance the performance of photocatalysis. The mechanism of photoactivity of the

obtained (Ti/Ce)UiO-66-X@TiO₂ hybrid materials is complicated and is probably due to electronic coupling, that is, the charge-transfer complex between UiO MOFs and TiO₂. Moreover, the presence of electron interactions between Ce-Ti species results in the formation of two redox mediators, Ce⁴⁺/Ce³⁺ and Ti⁴⁺/Ti³⁺, which promote the generation of more Lewis acid sites on the surface of the photocatalyst and produce an oxygen-rich environment around TiO₂. This research may stimulate some new ideas for employing a well-known matrix, such as TiO₂, and a new class of metal-organic frameworks to build novel and efficient heterostructure photocatalysts for environmental remediation, hydrogen generation, and other applications.

CRedit authorship contribution statement

Patrycja Parnicka: Resources, Conceptualization, Funding acquisition, Project administration, Investigation, Methodology, Visualization, Writing – original draft, Writing – review & editing. **Wojciech Lisowski:** Investigation, Visualization, Writing – original draft. **Tomasz Klimczuk:** Investigation, Writing – original draft. **Alicja Mikołajczyk:** Investigation, Visualization, Writing – original draft. **Adriana Zaleska-Medynska:** Resources, Supervision.

Declaration of Competing Interest

The authors declare the following financial interests/personal relationships which may be considered as potential competing interests: Patrycja Parnicka reports financial support was provided by National Science Centre Poland.

Acknowledgements

This research was supported by the Polish National Science Center under the grant titled “Novel REOF@TiO₂ nanomaterials with potential applications in photocatalytic processes” (contract No.: 2017/27/N/ST5/00738). The authors thank Patrycja Wilczewska for help with the chromium reduction measurements.

Appendix A. Supporting information

Supplementary data associated with this article can be found in the online version at [doi:10.1016/j.apcatb.2022.121349](https://doi.org/10.1016/j.apcatb.2022.121349).

References

- [1] A European strategic long-term vision for a prosperous, modern, competitive and climate neutral economy, Brussels, 28.11.2018, 2018. (<https://ec.europa.eu/>)

- transparency/regdoc/rep/1/2018/EN/COM-2018-773-F1-EN-MAIN-PART-1. PDF).
- [2] S.-W. Lv, Y. Cong, X. Chen, W. Wang, L. Che, Developing fine-tuned metal-organic frameworks for photocatalytic treatment of wastewater: a review, *Chem. Eng. J.* (2021), 133605, <https://doi.org/10.1016/j.cej.2021.133605>.
 - [3] S. Tasleem, M. Tahir, W.A. Khalifa, Current trends in structural development and modification strategies for metal-organic frameworks (MOFs) towards photocatalytic H₂ production: a review, *Int. J. Hydrog. Energy* 46 (2021) 14148–14189, <https://doi.org/10.1016/j.ijhydene.2021.01.162>.
 - [4] J.H. Cavka, S. Jakobsen, U. Olsbye, N. Guillou, C. Lamberti, S. Bordiga, K. P. Lillerud, A new zirconium inorganic building brick forming metal organic frameworks with exceptional stability, *J. Am. Chem. Soc.* 130 (2008) 13850–13851, <https://doi.org/10.1021/ja8057953>.
 - [5] Y.P. Yuan, L.S. Yin, S.W. Cao, G.S. Xu, C.H. Li, C. Xue, Improving photocatalytic hydrogen production of metal-organic framework UiO-66 octahedrons by dye-sensitization, *Appl. Catal. B Environ.* 168–169 (2015) 572–576, <https://doi.org/10.1016/j.apcatb.2014.11.007>.
 - [6] X. Qiu, Y. Zhu, X. Zhang, Y. Zhang, L.T. Menisa, C. Xia, S. Liu, Z. Tang, Cerium-based metal-organic frameworks explored with uio architecture for visible light-induced aerobic oxidation of benzyl alcohol, *Sol. RRL* 4 (2020) 1–7, <https://doi.org/10.1002/solr.201900449>.
 - [7] T.F. Chen, S.Y. Han, Z.P. Wang, H. Gao, L.Y. Wang, Y.H. Deng, C.Q. Wan, Y. Tian, Q. Wang, G. Wang, G.S. Li, Modified UiO-66 frameworks with methylthio, thiol and sulfonic acid function groups: the structure and visible-light-driven photocatalytic property study, *Appl. Catal. B Environ.* 259 (2019), 118047, <https://doi.org/10.1016/j.apcatb.2019.118047>.
 - [8] Y. Zhang, H. Chen, Y. Pan, X. Zeng, X. Jiang, Z. Long, X. Hou, Cerium-based UiO-66 metal-organic frameworks explored as efficient redox catalysts: titanium incorporation and generation of abundant oxygen vacancies, *Chem. Commun.* 55 (2019) 13959–13962, <https://doi.org/10.1039/c9cc06562h>.
 - [9] A. Wang, Y. Zhou, Z. Wang, M. Chen, L. Sun, X. Liu, Titanium incorporated with UiO-66(Zr)-type Metal-Organic Framework (MOF) for photocatalytic application, *RSC Adv.* 6 (2016) 3671–3679, <https://doi.org/10.1039/c5ra24135a>.
 - [10] H. Zhao, Z. Xing, S. Su, S. Song, Z. Li, W. Zhou, Gear-shaped mesoporous NH₂-MIL-53(Al)/CdS P-N heterojunctions as efficient visible-light-driven photocatalysts, *Appl. Catal. B Environ.* 291 (2021), 120106, <https://doi.org/10.1016/j.apcatb.2021.120106>.
 - [11] S. Mao, J.W. Shi, G. Sun, D. Ma, C. He, Z. Pu, K. Song, Y. Cheng, Au nanodots@thiol-UiO66@ZnIn₂S₄ nanosheets with significantly enhanced visible-light photocatalytic H₂ evolution: the effect of different Au positions on the transfer of electron-hole pairs, *Appl. Catal. B Environ.* 282 (2021), 119550, <https://doi.org/10.1016/j.apcatb.2020.119550>.
 - [12] S. Karamzadeh, E. Sanchooli, A.R. Oveisi, S. Daliran, R. Luque, Visible-LED-light-driven photocatalytic synthesis of N-heterocycles mediated by a polyoxometalate-containing mesoporous zirconium metal-organic framework, *Appl. Catal. B Environ.* 303 (2022), 120815, <https://doi.org/10.1016/j.apcatb.2021.120815>.
 - [13] M. Zhang, Q. Shang, Y. Wan, Q. Cheng, G. Liao, Z. Pan, Self-template synthesis of double-shell TiO₂@ZIF-8 hollow nanospheres via sonocrystallization with enhanced photocatalytic activities in hydrogen generation, *Appl. Catal. B Environ.* 241 (2019) 149–158, <https://doi.org/10.1016/j.apcatb.2018.09.036>.
 - [14] C.C. Wang, X. Wang, W. Liu, The synthesis strategies and photocatalytic performances of TiO₂/MOFs composites: a state-of-the-art review, *Chem. Eng. J.* 391 (2020), <https://doi.org/10.1016/j.cej.2019.123601>.
 - [15] B. Zhang, J. Zhang, X. Tan, D. Shao, J. Shi, L. Zheng, J. Zhang, G. Yang, B. Han, MIL-125-NH₂@TiO₂ core-shell particles produced by a post-solvothermal route for high-performance photocatalytic H₂ production, *ACS Appl. Mater. Interfaces* 10 (2018) 16418–16423, <https://doi.org/10.1021/acsami.8b01462>.
 - [16] Y. Xue, J. Lin, Y. Fan, A. Elsanousi, X. Xu, J. Mi, J. Li, X. Zhang, Y. Lu, T. Zhang, C. Tang, Controllable synthesis of uniformly distributed hollow rutile TiO₂ hierarchical microspheres and their improved photocatalysis, *Mater. Chem. Phys.* 143 (2013) 446–454, <https://doi.org/10.1016/j.matchemphys.2013.09.026>.
 - [17] S.L. Estes, M.R. Antonio, L. Soderholm, Tetraavalent Ce in the nitrate-decorated hexanuclear cluster [Ce₆(μ₃-O)₄(μ₃-OH)₄]¹²⁺: a structural end point for ceria nanoparticles, *J. Phys. Chem. C* 120 (2016) 5810–5818, <https://doi.org/10.1021/acs.jpcc.6b00644>.
 - [18] J.W. Furness, A.D. Kaplan, J. Ning, J.P. Perdew, J. Sun, Accurate and numerically efficient r2SCAN meta-generalized gradient approximation, *J. Phys. Chem. Lett.* 11 (2020) 8208–8215, <https://doi.org/10.1021/acs.jpcl.0c02405>.
 - [19] A.P. Bartók, J.R. Yates, Regularized SCAN functional, *J. Chem. Phys.* 150 (2019) 1–6, <https://doi.org/10.1063/1.5094646>.
 - [20] G. Kresse, J. Hafner, Ab initio molecular-dynamics simulation of the liquid-metalamorphous-semiconductor transition in germanium, *Phys. Rev. B* 49 (1994) 14251–14269, <https://doi.org/10.1103/PhysRevB.49.14251>.
 - [21] G. Kresse, J. Furthmüller, Efficiency of ab-initio total energy calculations for metals and semiconductors using a plane-wave basis set, *Comput. Mater. Sci.* 6 (1996) 15–50, [https://doi.org/10.1016/0927-0256\(96\)00008-0](https://doi.org/10.1016/0927-0256(96)00008-0).
 - [22] J.P. Perdew, K. Burke, M. Ernzerhof, Generalized gradient approximation made simple, *Phys. Rev. Lett.* 77 (1996) 3865–3868, <https://doi.org/10.1103/PhysRevLett.77.3865>.
 - [23] P. Parnicka, P. Mazierski, W. Lisowski, T. Klimczuk, J. Nadolna, A. Zaleska-Medynska, A new simple approach to prepare rare-earth metals-modified TiO₂ nanotube arrays photoactive under visible light: surface properties and mechanism investigation, *Results Phys.* 12 (2019) 412–423, <https://doi.org/10.1016/j.rinp.2018.11.073>.
 - [24] P. Wilczewska, A.E.N. Ona, A. Bielicka-Gieldoń, A. Malankowska, K. Tabaka, J. Ryl, F. Pniowski, E.M. Siedlecka, Application of BiOClBr photocatalyst to cytostatic drugs removal from water; mechanism and toxicity assessment, *Sep. Purif. Technol.* 254 (2021), 117601, <https://doi.org/10.1016/j.seppur.2020.117601>.
 - [25] V. Stavila, J. Volponi, A.M. Katzenmeyer, M.C. Dixon, M.D. Allendorf, Kinetics and mechanism of metal-organic framework thin film growth: systematic investigation of HKUST-1 deposition on QCM electrodes, *Chem. Sci.* 3 (2012) 1531–1540, <https://doi.org/10.1039/c2sc20065a>.
 - [26] L. Valenzano, B. Civalieri, S. Chavan, S. Bordiga, M.H. Nilsen, S. Jakobsen, K. P. Lillerud, C. Lamberti, Disclosing the complex structure of UiO-66 metal organic framework: a synergic combination of experiment and theory, *Chem. Mater.* 23 (2011) 1700–1718, <https://doi.org/10.1021/cm1022882>.
 - [27] M. Campanelli, T. Del Giacco, F. De Angelis, E. Mosconi, M. Taddei, F. Marmottini, F. Costantino, A Solvent Free Synthetic Route for Cerium(IV) Metal-Organic Frameworks with UiO-66 Architecture and Their Photocatalytic Application, 2019. doi:10.26434/chemrxiv.9199634.
 - [28] K. Hendrickx, D.E.P. Vanpoucke, K. Leus, K. Lejaeghere, A. Van Yperen-De Deyne, V. Van Speybroeck, P. Van Der Voort, K. Hemelsoet, Understanding intrinsic light absorption properties of UiO-66 frameworks: a combined theoretical and experimental study, *Inorg. Chem.* 54 (2015) 10701–10710, <https://doi.org/10.1021/acs.inorgchem.5b01593>.
 - [29] A.S. Yasin, J. Li, N. Wu, T. Musho, Study of the inorganic substitution in a functionalized UiO-66 metal-organic framework, *Phys. Chem. Chem. Phys.* 18 (2016) 12748–12754, <https://doi.org/10.1039/c5cp08070c>.
 - [30] E. Flage-Larsen, K. Thorshaug, Linker conformation effects on the band gap in metal-organic frameworks, *Inorg. Chem.* 53 (2014) 2569–2572, <https://doi.org/10.1021/ic4028628>.
 - [31] S. Chavan, J.G. Vitillo, D. Gianolio, O. Zavorotynska, B. Civalieri, S. Jakobsen, M. H. Nilsen, L. Valenzano, C. Lamberti, K.P. Lillerud, S. Bordiga, H₂ storage in isostructural UiO-67 and UiO-66 MOFs, *Phys. Chem. Chem. Phys.* 14 (2012) 1614–1626, <https://doi.org/10.1039/c1cp23434j>.
 - [32] K. Hendrickx, J.J. Joos, A. De Vos, D. Poelman, P.F. Smet, V. Van Speybroeck, P. Van Der Voort, K. Lejaeghere, Exploring lanthanide doping in UiO-66: a combined experimental and computational study of the electronic structure, *Inorg. Chem.* 57 (2018) 5463–5474, <https://doi.org/10.1021/acs.inorgchem.8b00425>.
 - [33] P. Parnicka, W. Lisowski, T. Klimczuk, J. Łuczak, A. Żak, A. Zaleska-Medynska, Visible-light-driven lanthanide-organic-frameworks modified TiO₂ photocatalysts utilizing up-conversion effect, *Appl. Catal. B Environ.* 291 (2021), <https://doi.org/10.1016/j.apcatb.2021.120056>.
 - [34] S. Öien, D. Wragg, H. Reinsch, S. Svelle, S. Bordiga, C. Lamberti, K.P. Lillerud, Detailed structure analysis of atomic positions and defects in zirconium metal-organic frameworks, *Cryst. Growth Des.* 14 (2014) 5370–5372, <https://doi.org/10.1021/cg501386j>.
 - [35] N. Ko, J. Hong, S. Sung, K.E. Cordova, H.J. Park, J.K. Yang, J. Kim, A significant enhancement of water vapour uptake at low pressure by amine-functionalization of UiO-67, *Dalton Trans.* 44 (2015) 2047–2051, <https://doi.org/10.1039/c4dt02582b>.
 - [36] M. Lammert, M.T. Wharmby, S. Smolders, B. Bueken, A. Lieb, K.A. Lomachenko, D. De Vos, N. Stock, Cerium-based metal organic frameworks with UiO-66 architecture: synthesis, properties and redox catalytic activity, *Chem. Commun.* 51 (2015) 12578–12581, <https://doi.org/10.1039/c5cc02606g>.
 - [37] A. Airi, C. Atzori, F. Bonino, A. Damin, S. Öien-Ødegaard, E. Aunan, S. Bordiga, A spectroscopic and computational study of a tough MOF with a fragile linker: Ce-UiO-66-ADC, *Dalton Trans.* 49 (2019) 12–16, <https://doi.org/10.1039/c9dt04112e>.
 - [38] T. Islamoglu, D. Ray, P. Li, M.B. Majewski, I. Akpinar, X. Zhang, C.J. Cramer, L. Gagliardi, O.K. Farha, From transition metals to lanthanides to actinides: metal-mediated tuning of electronic properties of isostructural metal-organic frameworks, *Inorg. Chem.* 57 (2018) 13246–13251, <https://doi.org/10.1021/acs.inorgchem.8b01748>.
 - [39] K.I. Hadjilivannov, D.A. Panayotov, M.Y. Mihaylov, E.Z. Ivanova, K.K. Chakarova, S. M. Andonova, N.L. Drenchev, Power of infrared and Raman spectroscopies to characterize metal-organic frameworks and investigate their interaction with guest molecules, *Chem. Rev.* 121 (2021) 1286–1424, <https://doi.org/10.1021/acs.chemrev.0c00487>.
 - [40] Y. Dong, L. Cao, J. Li, Y. Yang, J. Wang, Facile preparation of UiO-66/PAM monoliths: via CO₂-in-water HIFEs and their applications, *RSC Adv.* 8 (2018) 32358–32367, <https://doi.org/10.1039/c8ra05809a>.
 - [41] V. Zelenák, Z. Vargová, K. Györyová, Correlation of infrared spectra of zinc(II) carboxylates with their structures, *Spectrochim. Acta Part A Mol. Biomol. Spectrosc.* 66 (2007) 262–272, <https://doi.org/10.1016/j.saa.2006.02.050>.
 - [42] M. Kandiah, M.H. Nilsen, S. Usseglio, S. Jakobsen, U. Olsbye, M. Tilset, C. Larabi, E.A. Quadrelli, F. Bonino, K.P. Lillerud, Synthesis and stability of tagged UiO-66 Zr-MOFs, *Chem. Mater.* 22 (2010) 6632–6640, <https://doi.org/10.1021/cm102601v>.
 - [43] A. Van Yperen-De Deyne, K. Hendrickx, L. Vanduyfhuys, G. Sastre, P. Van Der Voort, V. Van Speybroeck, K. Hemelsoet, Vibrational fingerprint of the absorption properties of UiO-type MOF materials, *Theor. Chem. Acc.* 135 (2016) 1–14, <https://doi.org/10.1007/s00214-016-1842-8>.
 - [44] A.M. Ebrahim, Doping of Metal Organic Framework (UiO) and for NO₂ adsorption at ambient Conditions, CUNY Acad. Work, 2013.
 - [45] A. León, P. Reuquen, C. Garín, R. Segura, P. Vargas, P. Zapata, P.A. Orihuela, FTIR and raman characterization of TiO₂ nanoparticles coated with polyethylene glycol as carrier for 2-methoxyestradiol, *Appl. Sci.* 7 (2017) 1–9, <https://doi.org/10.3390/app7010049>.
 - [46] A. V. Naumkin, A. Kraut-Vass, C.J. Powell, S.W. Gaarenstroom, National Institute of Standards and Technology (U.S.), NIST X-ray Photoelectron Spectroscopy database 20. Version 4.1, 2012. doi:http://srdata.nist.gov/xps/.

- [47] E. Paparazzo, Use and mis-use of x-ray photoemission spectroscopy Ce 3d spectra of Ce_2O_3 and CeO_2 , *J. Phys. Condens. Matter* 30 (2018), <https://doi.org/10.1088/1361-648X/aad248>.
- [48] M. Romeo, K. Bak, J. El Fallah, F. Le Normand, L. Hilaire, XPS Study of the reduction of cerium dioxide, *Surf. Interface Anal.* 20 (1993) 508–512, <https://doi.org/10.1002/sia.740200604>.
- [49] A. Pfau, K.-D. Schierbaum, The electronic structure of stoichiometric and reduced CeO_2 surfaces: an XPS, UPS and HREELS study, *Surf. Sci.* 6028 (1994), [https://doi.org/10.1016/0039-6028\(94\)90027-2](https://doi.org/10.1016/0039-6028(94)90027-2).
- [50] Q. Liu, B. Zhou, M. Xu, G. Mao, Integration of nanosized ZIF-8 particles onto mesoporous TiO_2 nanobeads for enhanced photocatalytic activity, *RSC Adv.* 7 (2017) 8004–8010, <https://doi.org/10.1039/C6RA28277F>.
- [51] M. Thommes, K. Kaneko, A. V. Neimark, J.P. Olivier, F. Rodriguez-reinoso, J. Rouquerol, K.S.W. Sing, Physisorption of gases, with special reference to the evaluation of surface area and pore size distribution (IUPAC Technical Report), 2015, doi:10.1515/pac-2014-1117.
- [52] M.J. Katz, Z.J. Brown, Y.J. Colón, P.W. Siu, K.A. Scheidt, R.Q. Snurr, J.T. Hupp, O. K. Farha, A facile synthesis of UiO-66, UiO-67 and their derivatives, *Chem. Commun.* 49 (2013) 9449–9451, <https://doi.org/10.1039/c3cc46105j>.
- [53] X.P. Wu, L. Gagliardi, D.G. Truhlar, Cerium metal-organic framework for photocatalysis, *J. Am. Chem. Soc.* 140 (2018) 7904–7912, <https://doi.org/10.1021/jacs.8b03613>.
- [54] F. Mu, Q. Cai, H. Hu, J. Wang, Y. Wang, S. Zhou, Y. Kong, Construction of 3D hierarchical microarchitectures of Z-scheme UiO-66-(COOH)₂/ZnIn₂S₄ hybrid decorated with non-noble MoS_2 cocatalyst: a highly efficient photocatalyst for hydrogen evolution and Cr(VI) reduction, *Chem. Eng. J.* 384 (2020), 123352, <https://doi.org/10.1016/j.cej.2019.123352>.
- [55] X.H. Yi, S.Q. Ma, X.D. Du, C. Zhao, H. Fu, P. Wang, C.C. Wang, The facile fabrication of 2D/3D Z-scheme g-C₃N₄/UiO-66 heterojunction with enhanced photocatalytic Cr(VI) reduction performance under white light, *Chem. Eng. J.* 375 (2019), <https://doi.org/10.1016/j.cej.2019.121944>.
- [56] L. Li, Y. Xu, D. Zhong, Highly efficient adsorption and reduction of Cr(VI) ions by a Core-Shell Fe_3O_4 @UiO-66@PANI composite, *J. Phys. Chem. A* 124 (2020) 2854–2862, <https://doi.org/10.1021/acs.jpca.0c00269>.
- [57] W. Zhang, L. Wang, J. Zhang, Preparation of Ag/UiO-66-NH₂ and its application in photocatalytic reduction of Cr(VI) under visible light, *Res. Chem. Intermed.* 45 (2019) 4801–4811, <https://doi.org/10.1007/s11164-019-03865-6>.
- [58] Y.X. Li, X. Wang, C.C. Wang, H. Fu, Y. Liu, P. Wang, C. Zhao, S-TiO₂/UiO-66-NH₂ composite for boosted photocatalytic Cr(VI) reduction and bisphenol A degradation under LED visible light, *J. Hazard. Mater.* 399 (2020), 123085, <https://doi.org/10.1016/j.jhazmat.2020.123085>.
- [59] J.D. Evans, B. Garai, H. Reinsch, W. Li, S. Dissegna, V. Bon, I. Senkovska, R. A. Fischer, S. Kaskel, C. Janiak, N. Stock, D. Volkmer, Metal-organic frameworks in Germany: from synthesis to function, *Coord. Chem. Rev.* 380 (2019) 378–418, <https://doi.org/10.1016/j.ccr.2018.10.002>.
- [60] V. Kumaravel, M.D. Imam, A. Badreldin, R.K. Chava, J.Y. Do, M. Kang, A. Abdel-Wahab, Photocatalytic hydrogen production: role of sacrificial reagents on the activity of oxide, carbon, and sulfide catalysts, *Catalysts* 9 (2019), <https://doi.org/10.3390/catal9030276>.
- [61] B. Wang, J. Zhang, F. Huang, Enhanced visible light photocatalytic H₂ evolution of metal-free g-C₃N₄/SiC heterostructured photocatalysts, *Appl. Surf. Sci.* 391 (2017) 449–456, <https://doi.org/10.1016/j.apsusc.2016.07.056>.
- [62] N. Zhang, X. Zhang, C. Gan, J. Zhang, Y. Liu, M. Zhou, C. Zhang, Y. Fang, Heterostructural Ag₃PO₄/UiO-66 composite for highly efficient visible-light photocatalysts with long-term stability, *J. Photochem. Photobiol. A Chem.* 376 (2019) 305–315, <https://doi.org/10.1016/j.jphotochem.2019.03.025>.
- [63] Y. Li, B. Yang, B. Liu, MOF assisted synthesis of TiO₂/Au/Fe₂O₃ hybrids with enhanced photocatalytic hydrogen production and simultaneous removal of toxic phenolic compounds, *J. Mol. Liq.* 322 (2021), 114815, <https://doi.org/10.1016/j.molliq.2020.114815>.
- [64] M. Cao, F. Yang, Q. Zhang, J. Zhang, L. Zhang, L. Li, X. Wang, W.L. Dai, Facile construction of highly efficient MOF-based Pd@UiO-66-NH₂/ZnIn₂S₄ flower-like nanocomposites for visible-light-driven photocatalytic hydrogen production, *J. Mater. Sci. Technol.* 76 (2021) 189–199, <https://doi.org/10.1016/j.jmst.2020.11.028>.
- [65] A. Santiago-Portillo, S. Navalón, P. Concepción, M. Álvaro, H. García, Influence of terephthalic acid substituents on the catalytic activity of MIL-101(Cr) in three Lewis acid catalyzed reactions, *ChemCatChem* 9 (2017) 2506–2511, <https://doi.org/10.1002/cctc.201700236>.
- [66] L. Zhang, B.K. Miller, P.A. Crozier, Atomic level in situ observation of surface amorphization in anatase nanocrystals during light irradiation in water vapor, *Nano Lett.* 13 (2013) 679–684, <https://doi.org/10.1021/nl304333h>.
- [67] M.I. Cabrera, O.M. Alfano, A.E. Cassano, Absorption and scattering coefficients of titanium dioxide particulate suspensions in water, *J. Phys. Chem.* 100 (1996) 20043–20050, <https://doi.org/10.1021/jp962095q>.
- [68] R. Acosta-Herazo, M.Á. Mueses, G.L. Puma, F. Machuca-Martínez, Impact of photocatalyst optical properties on the efficiency of solar photocatalytic reactors rationalized by the concepts of initial rate of photon absorption (IRPA) dimensionless boundary layer of photon absorption and apparent optical thickness, *Chem. Eng. J.* 356 (2019) 839–849, <https://doi.org/10.1016/j.cej.2018.09.085>.
- [69] I. Grčić, G. Li Puma, Six-Flux Absorption-Scattering Models for Photocatalysis under Wide-Spectrum Irradiation Sources in Annular and Flat Reactors Using Catalysts with Different Optical Properties, Elsevier B.V., 2017, <https://doi.org/10.1016/j.apcatb.2017.04.014>.
- [70] L. Hurtado, R. Natividad, E. Torres-García, J. Farias, G. Li Puma, Correlating the photocatalytic activity and the optical properties of LiVMO₆ photocatalyst under the UV and the visible region of the solar radiation spectrum, *Chem. Eng. J.* 262 (2015) 1284–1291, <https://doi.org/10.1016/j.cej.2014.10.052>.
- [71] J. Colina-Márquez, F. MacHuca-Martínez, G.L. Puma, Radiation absorption and optimization of solar photocatalytic reactors for environmental applications, *Environ. Sci. Technol.* 44 (2010) 5112–5120, <https://doi.org/10.1021/es100130h>.
- [72] P. Parnicka, T. Grzyb, A. Mikolajczyk, K. Wang, E. Kowalska, N. Steinfeldt, M. Klein, P. Mazierski, A. Zaleska-medynska, J. Nadolna, Experimental and theoretical investigations of the influence of carbon on a Ho³⁺-TiO₂ photocatalyst with Vis response, *J. Colloid Interface Sci.* 549 (2019) 212–224, <https://doi.org/10.1016/j.jcis.2019.04.074>.
- [73] M. Bledowski, L. Wang, A. Ramakrishnan, O.V. Khavryuchenko, V. D. Khavryuchenko, P.C. Ricci, J. Strunk, T. Cremer, C. Kolbeck, R. Beranek, Visible-light photocurrent response of TiO₂-polyheptazine hybrids: evidence for interfacial charge-transfer absorption, *Phys. Chem. Chem. Phys.* 13 (2011) 21511–21519, <https://doi.org/10.1039/c1cp22861g>.
- [74] O. Kitao, Photoinduced electron transfer in dye-sensitized solar cells: modified Sakata-Hashimoto-Hiramoto model (MSHH), *J. Phys. Chem. C* 111 (2007) 15889–15902, <https://doi.org/10.1021/jp073645v>.
- [75] C. Creutz, B.S. Brunshwig, N. Sutin, Interfacial charge-transfer absorption: 3. Application to semiconductor - molecule assemblies, *J. Phys. Chem. B* 110 (2006) 25181–25190, <https://doi.org/10.1021/jp063953d>.
- [76] C. Hansch, A. Leo, R.W. Taft, A survey of Hammett substituent constants and resonance and field parameters, *Chem. Rev.* 91 (1991) 165–195, <https://doi.org/10.1021/cr00002a004>.